

1 Improving **Annual** Fine Mineral Dust Representation from the Surface to the
2 Column in GEOS-Chem 14.4.1

3 Dandan Zhang^{1*}, Randall V. Martin¹, Xuan Liu^{1,2}, Aaron van Donkelaar¹, Christopher R. Oxford¹,
4 Yanshun Li¹, Jun Meng³, Danny M. Leung⁴, Jasper F. Kok⁵, Longlei Li⁶, Haihui Zhu¹, Jay R. Turner¹, Yu
5 Yan¹, Michael Brauer⁷, Yinon Rudich⁸, and Eli Windwer⁸

6 ¹Department of Energy, Environmental and Chemical Engineering, Washington University in St.
7 Louis, St. Louis, Missouri 63130, United States

8 ²Scripps Institution of Oceanography, University of California San Diego, San Diego, California
9 92093, United States

10 ³Department of Civil and Environmental Engineering, Washington State University, Pullman,
11 Washington 99163, United States

12 ⁴Atmospheric Chemistry Observations and Modeling Laboratory, National Science Foundation
13 National Center for Atmospheric Research, Boulder, Colorado 80301, United States

14 ⁵Department of Atmospheric and Oceanic Sciences, University of California Los Angeles, Los
15 Angeles, California 90095, United States

16 ⁶Department of Earth and Atmospheric Sciences, Cornell University, Ithaca, New York 14853,
17 United States

18 ⁷School of Population and Public Health, University of British Columbia, Vancouver, British
19 Columbia V6T 1Z3, Canada

20 ⁸Department of Earth and Planetary Sciences, Weizmann Institute of Science, Rehovot 76100,
21 Israel

22 Correspondence to: Dandan Zhang (dandan.z@wustl.edu)

23

24 Abstract

25 Accurate representation of mineral dust remains a challenge for global air quality or climate
26 models due to inadequate parametrization of the emission scheme, removal mechanisms, and
27 size distribution. While various studies have constrained aspects of dust emission fluxes and/or
28 dust optical depth, [annual mean](#) surface dust concentrations still vary by factors of 5-10 among
29 models. In this study, we focus on improving the [annual](#) simulation of fine dust in the GEOS-Chem
30 chemical transport model, leveraging recent mechanistic understanding of dust source and
31 removal, and reconciling the size differences between models and ground-based measurements.
32 Specifically, we conduct sensitivity simulations using GEOS-Chem in its high performance
33 configuration (GCHP) version 14.4.1 to investigate the effects of mechanism or parameter updates,
34 [on annual mean concentrations](#). The results are evaluated by comparisons versus Deep Blue
35 satellite-based aerosol optical depth (AOD) and AErosol RObotic NETwork (AERONET) ground-
36 based AOD for total column abundance, and versus the Surface Particulate Matter Network
37 (SPARTAN) for [novel measurements of](#) surface PM_{2.5} dust concentrations. Reconciling modelled
38 geometric diameter versus measured aerodynamic diameter is important for consistent
39 comparison. The two-fold overestimation of surface fine dust in the standard model is alleviated by
40 [39%](#) without degradation of total column abundance by implementing a new physics-based dust
41 emission scheme with better spatial distribution. Further reduction by [20%](#) of the overestimation of
42 surface PM_{2.5} dust is achieved through reducing the mass fraction of emitted fine dust based on the
43 brittle fragmentation theory, and explicit tracking of three additional fine mineral dust size bins with
44 updated parametrization for below-cloud scavenging. Overall, these developments reduce the
45 normalized mean difference against surface fine dust measurements from SPARTAN from [94%](#) to
46 [35%](#), while retaining comparable skill of total column abundance against satellite and ground-
47 based AOD.

Deleted: .

Deleted: 36

Deleted: 16

Deleted: 73

Deleted: 21

48 1 Introduction

49 Mineral dust exerts significant impacts on air quality as the most abundant aerosol component by
50 mass globally ([Kok et al., 2021b](#)), on ecosystem health through nutrient transport and deposition
51 such as phosphorous (Bayon et al., 2024; Swap et al., 1992) and iron (Jickells et al., 2005), and on
52 climate through its direct scattering and absorbing of radiation and indirect modifications of cloud
53 properties (Kok et al., 2017; Liao and Seinfeld, 1998; Mahowald et al., 2014). Despite its

Deleted: (Kok et al., 2021)

importance, accurate representation of long-term concentrations of mineral dust remains a challenge for global air quality or climate models due to inadequate parametrization of the emission scheme (Darmenova et al., 2009; Kok, 2011; Leung et al., 2023), removal mechanisms (Jones et al., 2022; Petroff and Zhang, 2010; Ryu and Min, 2022; Wang et al., 2014b; Zhang and Shao, 2014; Zhang et al., 2001), and size distribution (Kok et al., 2017; Mahowald et al., 2014). Observational constraints from satellite have been applied to reduce the large uncertainty of simulated mineral dust and its emissions (Mytilinaios et al., 2023; Ridley et al., 2016). However, intercomparison projects with various models still suggest large variability within a factor of 2 for the annual mean total column abundance of mineral dust, with even larger variability in surface concentrations and deposition by factors of 5-10 (Huneus et al., 2011; Uno et al., 2006; Wu et al., 2020).

Deleted: (Huneus et al., 2011; Uno et al., 2006; Wu et al., 2020)...

In addition to total column observations, ground-level measurements of mineral dust offer another promising opportunity to understand mechanisms affecting the accuracy of the surface concentration simulation and the variable performance from the surface to the total column in intercomparison projects. The Surface PARTiculate mAtter Network (SPARTAN, <https://www.spartan-network.org/>, last access: 4 February 2025) is a globally distributed monitoring network that measures the chemical components of fine particulate matter (PM_{2.5}), including in arid environments (Liu et al., 2024; Snider et al., 2015). These ground-based measurements of mineral dust in PM_{2.5} offer new data to evaluate, understand, and improve fine dust simulation in global models.

Dust emissions play a central role in controlling the surface and total column abundance of mineral dust (Kok et al., 2014; Leung et al., 2023; Tian et al., 2021). The predicted spatial distribution of dust emissions particularly affects the downwind dust concentrations through long-range transport and deposition (Prospero, 1999). A new physics-based dust emission scheme (Leung et al., 2023) includes recent developments in the parametrization of the threshold of friction velocity for dust mobilization (Martin and Kok, 2018), combined drag partitioning effects due to rocks (Marticorena and Bergametti, 1995) and vegetation (Pierre et al., 2014a) for a better representation of exerted surface friction velocity (Leung et al., 2023), and intermittent dust mobilization due to high-frequency turbulence (Comola et al., 2019). This dust emission scheme has achieved better spatial correlations of dust column abundance against ground-based and satellite-derived dust optical depth in the Community Earth System Model version 2 (CESM2)

93 (Leung et al., 2023, 2024). However, the effects of these new developments of dust emission
94 scheme on the bias against ground-based measurements of surface fine dust concentrations are
95 less well known and require further investigation.

96 The source and removal of dust in the size bins used in dust parametrizations can vary by orders of
97 magnitude across the broad size range of mineral dust (Kok, 2011; Wang et al., 2014b; Zhang et al.,
98 2001). Accounting for this size heterogeneity among dust bins could enable better representation
99 of the global dust cycle. Prior studies have found an underestimation of coarse dust emissions and
100 an overestimation of fine dust (Cakmur et al., 2006; Kok, 2011; Kok et al., 2017). While various
101 studies have focused on developing the representation of coarse or super coarse dust (Kok et al.,
102 2017; Meng et al., 2022), investigation of the effects of different emission size distributions on
103 ambient fine dust are needed through comparison with in situ fine dust measurements. In addition,
104 the developments and improvements of parallel computing in air quality or climate models
105 (Eastham et al., 2018; Harris et al., 2020; Hu et al., 2018; Martin et al., 2022) offer computational
106 capabilities to extend dust size bins with explicit treatments that could enable better
107 representation of dust, especially with rapid variation in processes across different sizes. While the
108 parametrization of dry deposition has been revisited and evaluated against observations (Emerson
109 et al., 2020), below-cloud or washout scavenging has been generally limited to lumped treatments
110 for fine and coarse aerosols in the bulk models (Jones et al., 2022; Wang et al., 2011, 2014a).
111 Developments of the size-resolved parametrization for below-cloud (washout) scavenging (Wang et
112 al., 2014b) are promising to improve the wet deposition of fine dust, which is especially important
113 in distant downwind regions due to long-range transport.

114 Many studies have examined daily dust variability for the purpose of short-term prediction (Amato
115 et al., 2013; Tindan et al., 2023; Yu et al., 2021). Our study focuses on a different objective of
116 accuracy of annual mean concentrations.

117 In this study, we implement recent developments of a new dust emission scheme with further
118 refinements including the clay content and wetness in the topsoil layer; reducing the dust
119 emissions over wet, snow and vegetation covered land surfaces; while constraining the global and
120 regional source with satellite aerosol optical depth (AOD). We revisit the size distribution of emitted
121 dust, explicitly track mineral dust with geometric diameter less than 2 μm in four size bins, and
122 update the parametrization for size-resolved washout scavenging. We conduct sensitivity

Deleted: (Kok, 2011; Kok et al., 2017)

Deleted: over size ranges

Deleted: top soil

126 simulations using the GEOS-Chem chemical transport model in its high performance configuration
 127 (GCHP) to investigate the effects of these developments. We focus on improving the annual fine
 128 dust representation in GCHP from the surface to the column, by comparisons against ground-level
 129 fine dust measurements, and against the ground-based and satellite-retrieved AOD over dusty
 130 regions of the Sahara, the Middle East and Asia.

Deleted: for better agreement

131 2 Data sources and model description

132 2.1 Data sources

133 Ground-based AOD measurements are obtained from the Aerosol Robotic Network (AERONET)
 134 Version 3 Level 2 database with improved cloud screening (Giles et al., 2019). The median number
 135 of days with AERONET measurements is 168 days for each site. We average daily AERONET AOD to
 136 an annual mean in the year of 2018. We use satellite retrievals of AOD from the Deep Blue
 137 algorithm (Hsu et al., 2019) based on Collection 6.1 of the Moderate Resolution Imaging
 138 Spectroradiometer (MODIS) instrument aboard the satellite platforms of Terra with local overpass
 139 around 10:30 and of Aqua around 13:30, and the Version 2.0 Deep Blue aerosol global product of
 140 the Visible Infrared Imaging Radiometer Suite (VIIRS) instruments aboard the joint NASA/NOAA
 141 Suomi National Polar-orbiting Partnership (Suomi NPP) and NOAA-20 satellites with local overpass
 142 around 13:30 (Cao et al., 2014). We choose the Deep Blue aerosol product due to its optimization
 143 for the retrieval of aerosol properties over bright surfaces, which is typical over arid regions. We
 144 average daily Deep Blue aerosol data for the year 2018. Simulated AOD is coincidentally sampled
 145 with available daily Deep Blue AOD. We compare simulated AOD over mainly dusty regions
 146 (defined as $AOD_{Dust}/AOD > 0.5$ from simulations) against satellite and AERONET AOD to reduce
 147 the effects of errors in other AOD components and focus on the performance of mineral dust.

Deleted: all

Deleted: products

Deleted: at a daily basis.

Deleted: average

148 We use the Version 4.2 Level 3 gridded cloud-free tropospheric aerosol extinction profile product
 149 during daytime and nighttime of the last 15 years (2007–2021) retrieved from the Cloud–Aerosol
 150 Lidar with Orthogonal Polarization (CALIOP) on board the Cloud–Aerosol Lidar Infrared Pathfinder
 151 Satellite Observations (CALIPSO) satellite for climatological aerosol profiles (Young et al., 2018).

152 We use global ground-based data from the Surface Particulate Matter Network (SPARTAN;
 153 <https://www.spartan-network.org/>, last access: 4 February 2025) with filter-based $PM_{2.5}$ chemical
 154 composition data (Liu et al., 2024; Snider et al., 2015). Particles with aerodynamic diameter less

Formatted: Space Before: 6 pt, After: 6 pt

Deleted: Particles with aerodynamic diameter less than 2.5 μm are collected on Teflon filters using AirPhoton SS5 sampling stations with a sharp-cut cyclone (SCC) 1.829 that operates at a target flow rate of 5 liter per minute (Lpm) and analyzed for fine mineral dust concentrations using X-ray Fluorescence (XRF) and a global mineral dust equation (Equation (A1); Liu et al., 2022) including correction of attenuation effects due to mass loading. We use data from sites with at least 10 samples for the 5-year (2019–2023) period after the network began using XRF. The 5-year averaged surface fine dust concentrations from all 26 SPARTAN sites are listed in Table A1....

than 2.5 μm are collected on Teflon filters using AirPhoton SS5 sampling stations with a sharp-cut cyclone (SCC) 1.829 that operates at a target flow rate of 5 liter per minute (Lpm). The sampling station follows either a standard sampling protocol or the National Aeronautics and Space Administration (NASA) – Italian Space Agency (ASI) Multi-Angle Imager for Aerosols (MAIA) sampling protocol. Under the standard sampling protocol, $\text{PM}_{2.5}$ is collected at staggered 3-hour intervals over a 9-day period, generating a 24-hour $\text{PM}_{2.5}$ sample covering a full diel cycle. Under the MAIA sampling protocol, $\text{PM}_{2.5}$ is collected continuously for 24 hours from 9 am to 9 am at a mission-defined frequency, which has been typically every 3 days during the sampling periods used here. The starting dates for MAIA sites are listed in Table A1. SPARTAN samples are analyzed for fine mineral dust concentrations using X-ray Fluorescence (XRF) and a global mineral dust equation (Equation (A1); Liu et al., 2022) including correction of attenuation effects due to mass loading. The 5-year averaged surface fine dust concentrations from SPARTAN sites are listed in Table A1. We use data from sites with at least 10 samples for the 5-year (2019–2023) period after the network began using XRF with samples. A sensitivity analysis requiring at least 50 samples per site is also conducted. This study used 2,296 filters from 25 SPARTAN sites for a total of 10,072 observational days.

Ground-based observations of $\text{PM}_{2.5}$ dust over North America are constructed with a global dust equation (Equation (A1); Liu et al., 2022) and the elemental measurements from the Air Quality System (AQS) database for speciated $\text{PM}_{2.5}$ observations in the United States (https://aqs.epa.gov/aqsweb/airdata/download_files.html#Daily, last access: 8 April 2025) and from the National Air Pollution Surveillance Program in Canada (<https://donnees.az.ec.gc.ca/data/air/monitor/national-air-pollution-surveillance-naps-program/Data-Donnees/2018/?lang=en>, last access: 8 April 2025). The AQS database includes measurements from both the Interagency Monitoring of Protected Visual Environments (IMPROVE) and Chemical Speciation Network (CSN) networks.

2.2 GEOS-Chem chemical transport model

We use the GEOS-Chem chemical transport model (<http://www.geos-chem.org>, last access: 4 February 2025) in its high-performance configuration (Eastham et al., 2018) version 14.4.1 (The International GEOS-Chem User Community, 2024) with improved performance and usability (Martin et al., 2022). The model is driven by meteorological inputs from GEOS Forward Processing (GEOS-FP; <https://gmao.gsfc.nasa.gov/>, last access: 4 February 2025) with a fine resolution

Deleted: We use the GEOS-Chem chemical transport model (<https://geoschem.github.io/>, last access: 4 February 2025) in its high-performance configuration (Eastham et al., 2018) version 14.4.1 (The International GEOS-Chem User Community, 2024) with improved performance and usability (Martin et al., 2022). The model is driven by meteorological inputs from GEOS Forward Processing (GEOS-FP; <https://gmao.gsfc.nasa.gov/>, last access: 4 February 2025) with resolution $0.25^\circ \times 0.3125^\circ$ (~25 km) and 72 hybrid sigma-pressure vertical levels up to 0.01 hPa. ¶

215 0.25° × 0.3125° (~25 km) and 72 hybrid sigma-pressure vertical levels up to 0.01 hPa. GEOS-FP
216 uses dynamic near-real-time assimilation algorithms compared to consistent static assimilation
217 algorithms used in Modern-Era Retrospective analysis for Research and Applications Version 2
218 (MERRA-2; https://gmao.gsfc.nasa.gov/GMAO_products/, last access: 19 April 2025). We choose
219 GEOS-FP over MERRA-2 for this study since GEOS-FP offers finer resolution for dust emission
220 calculations.

221 GEOS-Chem simulates detailed oxidant-aerosol chemistry in the troposphere and stratosphere,
222 with gas-phase mechanism of HO_x-NO_x-BrO_x-VOC-O₃ chemistry (Bey et al., 2001; Wang et al.,
223 2021), coupled to aerosol chemistry for sulfate-nitrate-ammonium (SNA) aerosol (Park et al.,
224 2004), black carbon (BC) (Wang et al., 2014a), and primary and secondary organic aerosol (Pai et
225 al., 2020), sea salt (Jaeglé et al., 2011), and natural and anthropogenic dust (Fairlie et al., 2007;
226 Meng et al., 2021; Philip et al., 2017; Zhang et al., 2013). The gas-aerosol partitioning for SNA is
227 computed by the HETP v1.0 thermodynamic module (Miller et al., 2024). We use the simple,
228 irreversible, direct yield scheme for secondary organic aerosol production (Pai et al., 2020). The
229 effects of aerosol on photolysis rates are computed with relative humidity dependent aerosol size
230 distributions and optical properties for hydrophilic aerosols with improved parametrization for the
231 effective radii of inorganic and organic aerosols (Latimer and Martin, 2019; Ridley et al., 2012; Zhu
232 et al., 2023) and updated optical properties for aspherical hydrophobic mineral dust
233 (http://geoschemdata.wustl.edu/ExtData/CHEM_INPUTS/CLOUD_J/v2025-01/FIX_scat-aer.dat,
234 last access: 7 April 2025) for different dust size bins as calculated by Singh et al. (2024) using the T-
235 matrix method for an equiprobable mixture of prolate and oblate spheroids with varying aspect
236 ratios using complex refractive indices from Sinyuk et al. (2003).

237 The standard dry deposition scheme in GEOS-Chem accounts for gravitational settling,
238 aerodynamic resistance with respect to turbulent transport within the surface layer, and surface
239 resistance to particle-surface contact due to Brownian diffusion, impaction, and interception with
240 an observation constrained parametrization (Emerson et al., 2020; Zhang et al., 2001). Wet
241 deposition includes separate algorithms for scavenging in convective updrafts, and in-cloud and
242 below-cloud scavenging from precipitation (Liu et al., 2001; Wang et al., 2011, 2014a).

243 Emissions for GEOS-Chem are configured using the Harmonized Emissions Component (HEMCO)
244 module v3.9.1 (Lin et al., 2021). Global anthropogenic emissions are from the Community

Deleted: (Miller et al., 2024)

Deleted: mineral dust (Singh et al., 2024).

Deleted: The standard wet

Deleted: scheme

249 Emissions Data System (CEDS) v2 at $0.5^\circ \times 0.5^\circ$ resolution (Feng et al., 2020). Offline emissions of
 250 lightning NO_x (Murray et al., 2012), biogenic VOCs, soil NO_x , sea salt (Weng et al., 2020) and mineral
 251 dust (Sections 2.3 and 4.2) at $0.25^\circ \times 0.3125^\circ$ resolution are included to represent emission
 252 processes at the finest available resolution and to enable consistent emission fluxes across model
 253 resolutions. Open fire emissions are from the daily Global Fire Emissions Database (GFED) v4.1s
 254 (Giglio et al., 2013) at $0.25^\circ \times 0.25^\circ$ resolution. Other default emission inventories in GCHP v14.4.1
 255 include volcanic SO_2 emissions (Fisher et al., 2011), marine emissions of dimethylsulfide (DMS)
 256 (Breider et al., 2017) at $1^\circ \times 1^\circ$ resolution, and ammonia at $0.25^\circ \times 0.25^\circ$ resolution (Bouwman et
 257 al., 1997; Croft et al., 2016). We conduct GCHP simulations at C48 (~200 km) resolution for the full
 258 year of 2018 following a one-month spin-up.

259 2.3 Default dust emission scheme

260 The default dust emission scheme in GEOS-Chem (hereafter GC Dust) originally implemented by
 261 Fairlie et al. (2007) is based on the semi-empirical Mineral Dust Entrainment and Deposition
 262 (DEAD) emission scheme (Zender et al., 2003) and the GOCART topographical source function
 263 (Ginoux et al., 2001) updated to a fine resolution of $0.25^\circ \times 0.25^\circ$ (Meng et al., 2021). The total dust
 264 emission flux in $\text{kg m}^{-2} \text{s}^{-1}$ is calculated based on Zender et al. (2003) and Fairlie et al. (2007):

$$265 \quad F_d = C_g C_{NA} f_{bare} S \varphi Q_s \quad (1)$$

266 where C_g is a global scaling factor and C_{NA} is a regional scaling factor in North America for total
 267 annual emissions of $\sim 2000 \text{ Tg yr}^{-1}$ as optimized by Meng et al. (2021); f_{bare} is the bare ground
 268 fraction as specified in Zender et al. (2003) to reduce dust emissions over wet, snow and vegetation
 269 covered surfaces:

$$270 \quad f_{bare} = (1 - A_l - A_{wl})(1 - A_{snow}) \left(1 - \frac{\text{LAI}}{\text{LAI}_{thr}}\right) \quad (2)$$

271 where A_l , A_{wl} , and A_{snow} is the fraction of land covered by lakes, wetlands, and snow, respectively.
 272 LAI is the leaf area index, and LAI_{thr} is the threshold LAI to reduce the bare soil fraction due to
 273 vegetation cover, which is set to $0.3 \text{ m}^2 \text{ m}^{-2}$ by default.

274 S is a topographical source function (Ginoux et al., 2001) updated at fine resolution of $0.25^\circ \times 0.25^\circ$
 275 and multiplied by the fraction of bare surface within each grid cell (Meng et al., 2021); φ is the

Deleted:
where

Deleted: the GOCART

279 sandblasting efficiency to convert horizontal saltation flux to vertical dust flux (Marticorena and
280 Bergametti, 1995):

281
$$\varphi = 10^{13.4 f_{clay} - 4} \quad (3)$$

282 where f_{clay} is the clay content in the ~~topsoil~~ layer and ~~is set to a global constant value of 0.2 to~~
283 reduce excessive sensitivity of dust emission fluxes to f_{clay} (Zender et al., 2003). Q_s is the
284 horizontal saltation flux as described in Section A2.

285 **2.4 Size distribution of emitted dust**

286 The default size distribution of emitted dust in GEOS-Chem implemented by Zhang et al. (2013) is
287 based on the Brittle Fragmentation Theory (Kok, 2011) with ~~fitted~~ parameter values ~~for better~~
288 ~~agreement of~~ dust observations from the Interagency Monitoring of Protected Visual Environments
289 (IMPROVE) ground-based monitoring network in the United States:

290
$$\frac{dV_d}{d \ln D_d} = \frac{D_d}{c_V} \left[1 + \operatorname{erf} \left(\frac{\ln(D_d/\overline{D_s})}{\sqrt{2} \ln \sigma_s} \right) \right] \exp \left[- \left(\frac{D_d}{\lambda} \right)^3 \right] \quad (4)$$

291 where V_d is the normalized volume for emitted dust aerosols in diameter of D_d in μm ; c_V is the
292 normalization constant to make the integration total of V_d of 1; $\overline{D_s} = 3.4 \mu\text{m}$ is the median diameter
293 of soil particles; $\sigma_s = 3.0$ is the geometric standard deviation of soil particles; λ is the side crack
294 propagation length, whose value is $8 \mu\text{m}$ in the default particle size distribution (PSD) used in the
295 GEOS-Chem (GC PSD), and is $12 \mu\text{m}$ in the Kok PSD (Kok, 2011).

296 Table 1. The binning of mineral dust in 4-bin and 7-bin simulations using GEOS-Chem. The
297 geometric diameter range is listed in the bracket adjacent to each size bin in unit of μm .

4-bin simulation	7-bin simulation
	DSTbin1 (0.2–0.36)
DST1 (0.2–2.0)	DSTbin2 (0.36–0.6)
	DSTbin3 (0.6–1.2)
	DSTbin4 (1.2–2.0)
DST2 (2.0–3.6)	DSTbin5 (2.0–3.6)
DST3 (3.6–6.0)	DSTbin6 (3.6–6.0)
DST4 (6.0–12.0)	DSTbin7 (6.0–12.0)

Deleted: top soil
Deleted: is used
Formatted: Font: +Body (Aptos)

Deleted: optimized using

301

302 Dust aerosols are conventionally separated into several dust bins to compromise between
 303 accuracy and computational expense (Ginoux et al., 2001; Zender et al., 2003). Table 1
 304 summarizes the binning of mineral dust in 4-bin and 7-bin simulations. In the GEOS-Chem
 305 standard bulk configuration used here, 4 dust size bins are used including DST1 to DST4 covering
 306 geometric diameter of 0.2–12.0 μm (Fairlie et al., 2007). For DST1, 4 sub-bins of 0.2–0.36 μm , 0.36–
 307 0.6 μm , 0.6–1.2 μm , and 1.2–2.0 μm are further separated for heterogeneous chemistry and AOD
 308 calculations, with shared emission, transport and deposition altogether as DST1 (Fairlie et al.,
 309 2007). To improve submicron dust representation, we implement full separation of the 7 dust bins
 310 for coupled physical and chemical processes in GEOS-Chem, as discussed in Section 4.3.2.

311 2.5 Reconciling geometric and aerodynamic diameter

312 A recent study has emphasized the importance of reconciling the geometric diameter used in
 313 models and the aerodynamic diameter used in ground-based measurements, especially for
 314 mineral dust with higher particle density of $\sim 2500 \text{ kg m}^{-3}$ than the standard density of 1000 kg m^{-3}
 315 and with aspherical shapes observed in the atmosphere (Huang et al., 2021). We harmonize the
 316 differences between geometric diameter and aerodynamic diameter based on Reid et al. (2003):

$$317 \quad D_{aer} = D_{geo} \sqrt{\frac{\rho_d}{\chi \rho_0}} \quad (5)$$

318 where D_{aer} is the aerodynamic diameter; D_{geo} is the geometric diameter; $\rho_d = 2500 \text{ kg m}^{-3}$ is the
 319 dust density; $\rho_0 = 1000 \text{ kg m}^{-3}$ is the standard spherical particle density; χ is the dynamic shape
 320 factor calculated by $\chi = \frac{1}{2} \left(F_s^{1/3} + \frac{1}{F_s^{1/3}} \right)$ and F_s is Stokes form factor (Bagheri and Bonadonna,
 321 2016; Huang et al., 2020) which can be calculated by $\text{HWR} \left(\frac{1}{\text{AR}} \right)^{1.3}$ where $\text{AR} = 1.70 \pm 0.03$ is the
 322 particle length to width ratio, and $\text{HWR} = 0.40 \pm 0.07$ is the particle height to width ratio (Huang et
 323 al., 2021). With this conversion, the aerodynamic diameter of 2.5 μm corresponds to the geometric
 324 diameter of 1.7 μm . The mass fraction of each simulated dust size bin to the total fine dust mass
 325 concentrations can be calculated by the integration of the dust size distribution of Equation (4) with
 326 the λ value of 8 μm of the default PSD used in the GEOS-Chem (GC PSD), which is 68% of DST1
 327 with diameter of 0.2–2.0 μm .

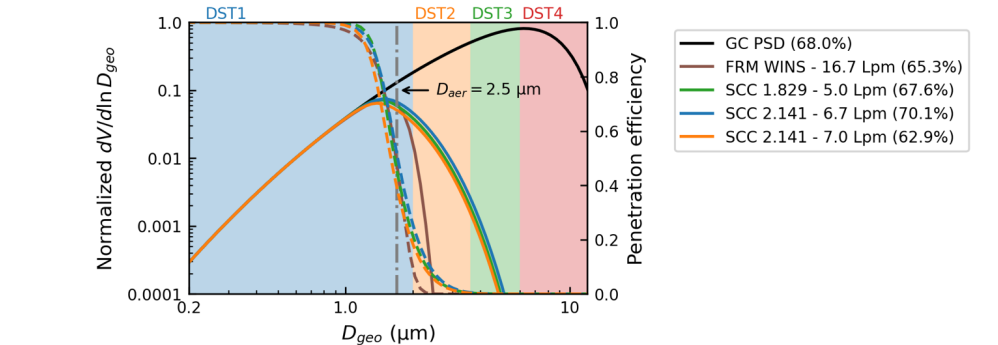
Deleted: Table 1

Deleted: 12

330 In addition to harmonizing different size types used in models and measurements, prior studies
 331 also suggested that the sharpness of size cut-off of different inlets used to collect $PM_{2.5}$ samples
 332 can affect the measured concentrations (Kenny et al., 2000; Peters et al., 2001). To evaluate the
 333 effects, we obtain the dust size distributions of different inlets by multiplying their penetration
 334 efficiencies (Peters et al., 2001) and GC PSD (Equation (4)).

335 Figure 1 shows the effects of the sharpness of size cut on the size distribution of collected dust
 336 $PM_{2.5}$ samples. All four inlets have a penetration efficiency of near unity for dust with geometric
 337 diameter less than $1.0\ \mu m$, which diminishes to 0.5 at a geometric diameter of $1.7\ \mu m$ and further
 338 diminishes with increasing diameter. The Well Impactor Ninety-Six (WINS) referenced by the
 339 Federal Reference Method (FRM) exhibits the sharpest size cut. The corresponding dust PSD is
 340 sharply attenuated for geometric diameters greater than $1.7\ \mu m$. The resultant effects on the mass
 341 fractions of the dust size bin to be included in dust $PM_{2.5}$ are small, with the mass fraction of DST1
 342 ranging from 65–70%. The mass fraction based on SCC 1.829 as used by SPARTAN differs by only
 343 -0.4% from that based on the original GC PSD without inlet penetration correction. In our Base
 344 simulation using the standard version of GEOS-Chem, we calculate surface $PM_{2.5}$ dust as 67.6% of
 345 DST1 to account for both aerodynamic diameter and inlet collection efficiency. Neglect of these
 346 effects would have increased simulated $PM_{2.5}$ dust concentrations by a factor of 2.

Deleted: Figure 1



348 Figure 1. Normalized particle size distribution (PSD) used by default in GEOS-Chem (GC PSD) in
 349 solid black with left axis; penetration efficiencies for different types of $PM_{2.5}$ inlets shown in dashed
 350 colored lines with right axis, including the Well Impactor Ninety-Six (WINS), and three types of
 351 Sharp-Cut Cyclone (SCC) inlets; Solid colored lines show the adjusted GC PSD collected by

different inlets. Grey dash-dotted line indicates the corresponding geometric diameter of 1.7 μm for the aerodynamic diameter of 2.5 μm . Filled rectangles indicate size ranges of 4 dust size bins. Percentages adjacent to GC PSD and different inlets are mass fractions of DST1 for the calculation of $\text{PM}_{2.5}$ dust concentrations.

3 Strong overestimation of surface fine dust

Figure 2 shows the spatial distributions of the annual total column AOD and surface $\text{PM}_{2.5}$ dust from AERONET, SPARTAN, and the Base simulation using the standard version of GEOS-Chem in the year of 2018. Mineral dust largely determines the AOD in AERONET and GEOS-Chem over and downwind of the main dust source regions including the Sahara, Middle East, and the Taklamakan and Gobi deserts in Asia. The simulated AOD over dusty regions ($\text{simulated AOD}_{\text{Dust}}/\text{AOD} > 0.5$) exhibits a high degree of consistency versus the ground-based observations of AERONET AOD with the regression slope near unity and R^2 of 0.7. However, the simulated surface $\text{PM}_{2.5}$ dust exhibits a pronounced overestimation by a factor of 2.4 compared to the ground-based measurements of SPARTAN. Simulated $\text{PM}_{2.5}$ dust is overestimated at the dusty sites of Abu Dhabi in the United Arab Emirates by 163%, Ilorin in Nigeria by 108%, and Kanpur in India by 96%.

Figure 3 shows the vertical profile of the aerosol extinction normalized by AOD over the main dust source regions and associated downwind regions, to understand the significant performance difference between the surface and the column, with the absolute extinction profile shown in Figure A1. The simulated vertical profile exhibits overall agreement against the 15-year (2007 to 2021) climatological mean extinction vertical profile from the CALIOP, with no evidence of a model overestimate in the lower mixed layer versus aloft, indicating the vertical distribution of mineral dust is not the main driver of the performance discrepancy between the surface and the column. However, further evaluations of the vertical profile near the surface are needed as CALIOP retrievals are challenging at lower altitudes especially below 100 m.

Deleted: defined here as

Deleted: 2

Deleted: 143

Deleted: 100

Deleted: 75

Deleted: Figure 3

Deleted: .

Deleted: shows excellent

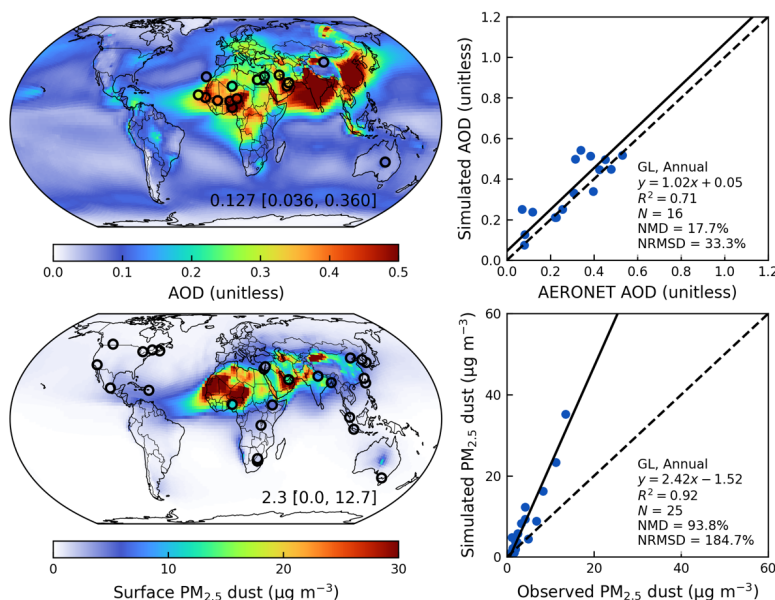
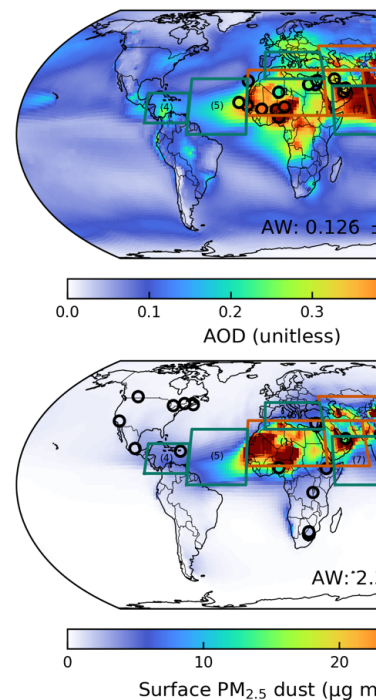


Figure 2. Annual simulated aerosol optical depth (AOD) and comparison against ground-based observations from AERONET over dusty regions ($\text{simulated AOD}_{\text{dust}} / \text{AOD} > 0.5$) (top) in the year of 2018; Annual simulated surface $\text{PM}_{2.5}$ dust and comparison against ground-based measurements from SPARTAN (bottom) from the Base simulation in the year of 2018. Filled circles on the maps represent ground-based observations from SPARTAN and AERONET. Inset values at the bottom right of the maps are $\text{arithmetic mean with 5}^{\text{th}}$ and 95^{th} percentiles in the square brackets. Regression statistics including reduced-major-axis linear regression equation, coefficient of variation (R^2), total number of points (N), normalized mean difference (NMD), and normalized root-mean-square difference (NRMSD) are listed at the bottom right of the scatter plots. Major source regions over land are outlined in red including: 1) the Sahara – SA, 2) Middle East – ME, and 3) Asia – AS. Major dust outflow regions over ocean are outlined in green including: 4) the Caribbean Sea – CRB, 5) the tropical Atlantic Ocean – TAT, 6) the Mediterranean Sea – MED, 7) the Arabian Sea – ARB, 8) the tropical Indian Ocean and the Bay of Bengal – IND, and 9) the northwestern Pacific Ocean – NWP.



Deleted:

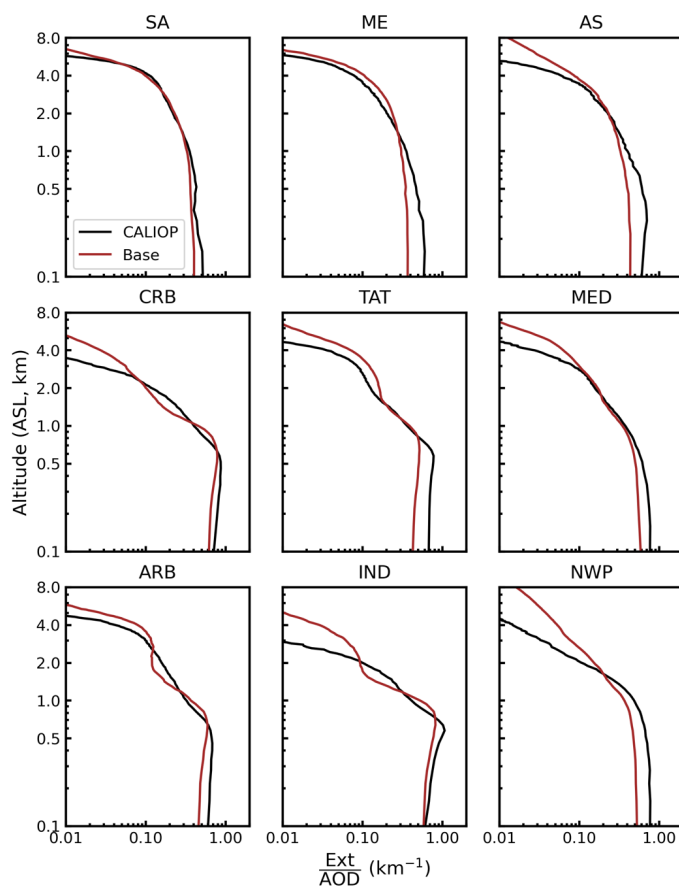
Deleted: $\text{AOD}_{\text{Dust}} / \text{AOD}$

Deleted:);

Deleted: area-weighted (AW)

Deleted: standard deviation

Deleted: Sean



406

407 Figure 3. Comparisons of the annual extinction vertical profile normalized by total column aerosol
 408 optical depth from the Base simulation in the year of 2018 against the 15-year (2007 to 2021)
 409 climatological mean extinction vertical profile from the CALIOP over different regions including the
 410 major dust source regions over land of the Sahara – SA, Middle East – ME, and Asia – AS, and the
 411 major dust outflow regions over ocean of the Caribbean Sea – CRB, the tropical Atlantic Ocean –
 412 TAT, the Mediterranean Sea – MED, the Arabian Sea – ARB, the tropical Indian Ocean and the Bay of
 413 Bengal – IND, and the northwestern Pacific Ocean – NWP.

414 **4 Model revisions to reduce the overestimation of surface fine mineral dust**

415 To reduce the overestimation of surface $\text{PM}_{2.5}$ dust, we 1) implement a new dust emission scheme
416 with further refinements for soil properties including the clay content and soil wetness in the top
417 soil layer and the threshold of leaf area index, 2) revisit the size distribution of emitted dust, 3)
418 explicitly track dust with geometric diameter less than $2\ \mu\text{m}$ in four size bins, and 4) update the
419 parametrization for size-resolved below-cloud scavenging.

420 **4.1 Sensitivity simulation setup**

421 Figure 4 summarizes the setup of sensitivity simulations to evaluate the effects of algorithmic
422 modifications and their performance versus satellite-retrieved AOD and surface dust
423 measurements. The default dust simulation (Base) in GEOS-Chem as implemented by Fairlie et al.
424 (2007) uses the DEAD emission scheme (Zender et al., 2003) with a topographical source function
425 (Ginoux et al., 2001; Meng et al., 2021) for natural dust (GC Dust) with 4 dust size bins for emission,
426 transport and removal with 7 dust size bins for dust optical depth calculation and heterogeneous
427 chemistry. To improve the spatial distributions of dust total column abundance, we implement a
428 new dust emission scheme developed by Leung et al. (2023) (DustL23; Emis). Additional
429 modifications on top of the original DustL23 emission scheme include 1) reducing the sensitivity of
430 soil clay content by eliminating the multiplication of the factor of the capped soil clay content f'_{clay}
431 (EmisClay); 2) halving the topmost soil wetness in the layer of 0-5 cm to approximate the soil
432 wetness in the top 1-2 cm layer which is most pertinent to dust emissions (Darmenova et al., 2009;
433 Wu et al., 2022) (EmisClayWet); and 3) reducing the threshold of LAI_{thr} from $1.0\ \text{m}^2\ \text{m}^{-2}$ to $0.5\ \text{m}^2\ \text{m}^{-2}$
434 (EmisClayWet LAI_{thr} or Emis*). To further improve the surface fine dust simulation, we update the
435 GEOS-Chem particle size distribution (PSD) with the PSD developed by Kok et al. (2011)
436 (Emis*PSD) with a larger value for the side crack propagation length of λ (12 μm versus 8 μm) which
437 reduced the mass fraction of emitted fine dust. The Kok PSD was shown to have excellent
438 agreement versus various soil size measurements (Kok, 2011), especially for fine dust distributions
439 (González-Flórez et al., 2023). Lastly, we allow for the four dust bins with geometric diameter less
440 than $2\ \mu\text{m}$ to have separate emission, transport, and dry and wet deposition while halving
441 anthropogenic dust emissions from AFCID (Emis*PSD7Bins0.5AD), and with updated below-cloud
442 or washout scavenging parametrization (Emis*PSD7Bins0.5ADWetDep). Each of these changes is
443 examined below.

The total global annual source strength for each sensitivity simulation is scaled to achieve unity slope versus Deep Blue AOD (Figure A2) over major dust source regions. The surface $PM_{2.5}$ dust concentrations are calculated by accounting for aerodynamic diameter and inlet penetration efficiency (Section 2.5) as 0.676 DST1 for 4-bin simulations, and DSTbin1 + DSTbin2 + DSTbin3 + 0.546 DSTbin4 for 7-bin simulations. We focus our evaluation on the skill in representing in situ $PM_{2.5}$ dust concentrations measured by SPARTAN, and in representing the spatial variation in annual mean AOD. Regression equations are calculated using reduced-major-axis linear regression (Smith, 2009) to account for uncertainties in both simulations and measurements.

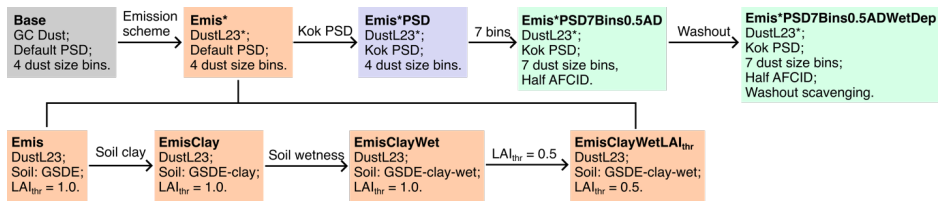


Figure 4. Sensitivity simulation setup. The grey box indicates default settings with the default dust emission scheme used in GEOS-Chem (GC Dust) with 4 dust size bins (Base). The orange box indicates the implementation of a modified dust scheme based on DustL23 (Emis*). Modifications based on the original DustL23 scheme with the soil texture dataset from the Global Soil Dataset for use in Earth System Models (GSDE) (Emis) include the soil clay content (EmisClay), soil wetness (EmisClayWet), and threshold leaf area index (EmisClayWetLAI_{thr}). The simulation setup for EmisClayWetLAI_{thr} is the same as that for Emis*. The blue box indicates the modification of size distribution of emitted dust (Emis*PSD). The green boxes indicate the improvements for fine dust including explicit tracking of dust with diameter less than 2 μm with a total of 7 dust size bins with halved anthropogenic fugitive, combustion, and industrial dust (AFCID) emissions (Emis*PSD7Bins0.5AD), and updating below-cloud (washout) scavenging coefficients (Emis*PSD7Bins0.5ADWetDep).

4.2 Improving the spatial distribution of mineral dust with updated emission scheme

We implement into GEOS-Chem a new physics-based dust emission scheme developed by Leung et al. (2023) (DustL23) to replace the default dust emission scheme (Section 2.3) used in GEOS-Chem (GC Dust). The spatial distributions of DustL23 in the Community Earth System Model version 2 (CESM2) exhibited better correlation against dust optical depth datasets and AERONET

Deleted: Figure A1

471 AOD than the DEAD scheme (Leung et al., 2024). We modify DustL23 for implementation into
 472 GEOS-Chem by 1) reducing dust emissions over wet, snow, and vegetation covered surfaces of
 473 semi-arid regions using Equation (7) below, 2) eliminating the multiplication of the capped clay
 474 content of the topsoil in Equation (8) below, 3) halving the soil wetness in the layer of 0-5 cm to
 475 represent the soil wetness in the top 1-2 cm layer which is most pertinent to dust emissions
 476 (Darmenova et al., 2009; Wu et al., 2022), 4) applying a regional scaling factor of 0.6 over the
 477 Sahara to reduce its emissions (Equation (8)), and 5) scaling the global total emission flux to
 478 achieve unity regression slope of simulated AOD versus Deep Blue AOD over dusty regions.

479 We begin with the formulation for total dust emission flux F_d in $\text{kg m}^{-2} \text{s}^{-1}$ following Leung et al.
 480 (2024):

$$481 \quad F_d = \eta C_{tune} C_d f_{bare} f'_{clay} \frac{\rho_a (u_{*s}^2 - u_{*it}^2)}{u_{*st}} \left(\frac{u_{*s}}{u_{*it}} \right)^\kappa \text{ for } u_{*s} > u_{*it} \quad (6)$$

482 where η is an intermittency factor, C_{tune} is a global tuning factor for the emission strength, C_d is the
 483 time-varying soil erodibility coefficient, f_{bare} is the bare ground fraction, f'_{clay} is the clay content in
 484 the topmost soil layer of f_{clay} capped at 0.2, ρ_a is the surface air density in kg m^{-3} , u_{*s} is the soil
 485 surface friction velocity in m s^{-1} corrected from the surface friction velocity of u_* by the drag
 486 partitioning effects of F_{eff} , u_{*it} is the dynamic or impact threshold friction velocity in m s^{-1} , u_{*st} is
 487 the standardized wet fluid threshold friction velocity in m s^{-1} , and κ is the fragmentation exponent.

488 We use u_{*st} in the denominator of Equation (6) following Kok et al. (2014) instead of u_{*it} following
 489 Leung et al. (2023) for tuning purpose. The parametrization details for these factors following Leung
 490 et al. (2023) can be found in Appendix Section A3.

491 We modify the DustL23 scheme (Leung et al., 2023) by adopting the equation for the bare ground
 492 fraction in Zender et al. (2003) to reduce dust emissions over wet, snow and vegetation covered
 493 surfaces with the dry erodible land fraction taken from satellite-based land cover:

$$494 \quad f_{bare} = A_{erod} (1 - A_{snow}) \left(1 - \frac{\text{LAI}}{\text{LAI}_{thr}} \right) \quad (7)$$

495 where A_{erod} is the area fraction of erodible surfaces including barren and sparsely vegetated land
 496 cover taken from the MODIS Land Cover Climate Modeling Grid (CMG) (MCD12C1) Version 6.1 data
 497 product; A_{snow} is the area fraction of snow cover, LAI is the leaf area index (Yuan et al., 2011), and

Deleted: surface

Formatted: Font: +Body (Aptos)

Deleted: Note that we

Formatted: Font: +Body (Aptos)

Formatted: Font: +Body (Aptos)

Formatted: Font: +Body (Aptos)

LAI_{thr} is the threshold LAI to reduce the bare soil fraction due to vegetation cover. We set an intermediate value of LAI_{thr} = 0.5 m² m⁻² instead of 1.0 m² m⁻² in Leung et al. (2023) to represent the reduction in dust emissions from sparse vegetation over semi-arid regions, which is more similar to the value of 0.3 used in prior work (Mahowald et al., 1999; Zender et al., 2003).

The enhancement factor $f_m \geq 1$ for the wet fluid threshold friction velocity due to soil wetness is calculated using Equations (A8) and (A9), but with spatially varying clay content f_{clay} in the topsoil layer. The gridded f_{clay} dataset is taken from the Global Soil Dataset for use in Earth System Models (GSDE) with various inputs from global and regional soil database (Shangguan et al., 2014), rather than the machine-learning trained Soil Grids v2.0 dataset with very few observations over arid regions (Poggio et al., 2021) used in Leung et al. (2023). In addition, we reduce the effects of clay content on dust emissions by eliminating the multiplication of the capped clay content f'_{clay} . Soil wetness is taken from the parent meteorological inputs of GEOS-FP (Koster et al., 2020) which targets the top 5 cm layer that desiccates more slowly following precipitation than the soil wetness in the top 1-2 cm layer (Swenson and Lawrence, 2014) that is most pertinent to dust emissions; we halve the soil wetness in an attempt to represent this process (Darmenova et al., 2009; Wu et al., 2022).

The global scaling factor C_{tune} is determined by the reduced-major-axis linear regression slope of simulated AOD versus satellite-retrieved AOD over dusty regions ($\frac{AOD_{dust}}{AOD} > 0.5$) in this study to constrain the intensity of dust emissions, whose values corresponding to different emission schemes are listed in Table A2. Additionally, a regional scaling factor of 0.6 over the Sahara (C_{sah}) and unity elsewhere is applied to reduce regionally excessive dust emissions that may be influenced by the tendency for global models to overrepresent emissions from large source regions compared with smaller sources (Kok et al., 2021a; Zhao et al., 2022).

The final formulation for dust emission flux is:

$$F_d = \eta C_{sah} C_{tune} C_d f_{bare} \frac{\rho_a (u_{*s}^2 - u_{*it}^2)}{u_{*st}} \left(\frac{u_{*s}}{u_{*it}} \right)^\kappa \text{ for } u_{*s} > u_{*it} \quad (8)$$

The calculated offline hourly dust emissions at $0.25^\circ \times 0.3125^\circ$ resolution using Equation (8) are then used to drive GCHP simulations at C48 resolution. The spatial distributions predicted from different emission schemes are evaluated against satellite-based Deep Blue AOD, ground-based

Deleted: top soil

Deleted: sensitivity

Deleted: to clay content

Deleted: , targeted at the top 5 cm layer, and is reduced by half to approximate the soil wetness in the top 1-2 cm layer which is most pertinent to dust emissions (Darmenova et al., 2009; Wu et al., 2022)

Deleted: Table A2. Additionally, a regional scaling factor of 0.6 over the Sahara (C_{sah}) and unity elsewhere is applied to reduce regionally excessive dust emissions.

538 AERONET AOD, and SPARTAN surface PM_{2.5} dust measurements.

539 Figure 5 shows the spatial distributions of annual dust emission fluxes and dust optical depth
540 predicted from different emission schemes, with Figure 6 showing the comparisons against Deep
541 Blue satellite AOD globally and over major dust source regions. Comparison of the Base and Emis
542 schemes reveals that the latter captures more secondary dust emission spots, especially over the
543 Sahara, and inland dust sources in Saudi Arabia. However, the comparison against Deep Blue AOD
544 over the Sahara is degraded versus the default scheme (Figure 6). As suggested by prior studies,
545 soil clay content is an important factor affecting the threshold friction velocity (Fécan et al., 1999;
546 Tian et al., 2021; Zender et al., 2003) and sandblasting efficiency (Zender et al., 2003), and is often
547 tuned for the optimization of dust emissions (Leung et al., 2024; Tian et al., 2021). Eliminating the
548 multiplication of the capped clay content of f'_{clay} reduces the effects of the clay content,
549 increasing emissions from the Bodélé Depression in Chad and El Djouf across the border of
550 Mauritania and Mali over the Sahara, from the Rub' al Khali desert in the inland Saudi Arabi, and
551 Taklamakan desert in the northwest China (Figure 5, EmisClay). Correspondingly, the R^2 from the
552 linear regression against Deep Blue AOD is improved from 0.60 to 0.70 over the Sahara, from 0.68
553 to 0.77 over the Middle East, and from 0.35 to 0.56 over Asia (Figure 6). The other two modifications
554 of halving soil wetness (EmisClayWet) and setting LAI_{thr} to 0.5 m² m⁻² (EmisClayWetLAI_{thr}) slightly
555 improve the spatial distribution of dust emissions by reducing the underestimation in Asia while
556 retaining the agreements in the Sahara and Middle East (Figure 6). Using the same dusty region of
557 the Base (Figure A3) or EmisClayWetLAI_{thr} (Figure A4) scheme for the comparisons of all dust
558 emission schemes versus Deep Blue AOD confirms similarly slight improvements of regional dust
559 emissions. Together these refinements exhibit comparable global performance as the Base
560 simulation versus Deep Blue AOD with improvements to the relative regional magnitude of dust
561 across the Sahara, Middle East and Asia as indicated by more comparable regression slopes
562 (Figure 6).

563 Figure 7 shows the evaluation of the Emis* (or EmisClayWetLAI_{thr}) simulation with ground-based
564 observations from AERONET and SPARTAN. The overestimation of surface PM_{2.5} dust against the
565 ground-based measurements of SPARTAN is reduced from 94% (Figure 2) to 55% (Figure 7),
566 reflecting regional improvements of the spatial distributions especially over the Middle East (Figure
567 6). The skill in representing AOD in the Emis* simulation remains comparable to that in the Base
568 simulation shown in Figure 2.

Deleted: Figure 5

Deleted: Figure 6

Deleted: Figure 6).

Formatted: Font: +Body (Aptos)

Deleted: dust emission sensitivity to

Deleted: Figure 5

Deleted: Figure 6).

Deleted: Figure 6).

Formatted: Font: +Body (Aptos)

Formatted: Font: +Body (Aptos)

Formatted: Font: +Body (Aptos)

Deleted: (Figure A2).

Formatted: Font: +Body (Aptos)

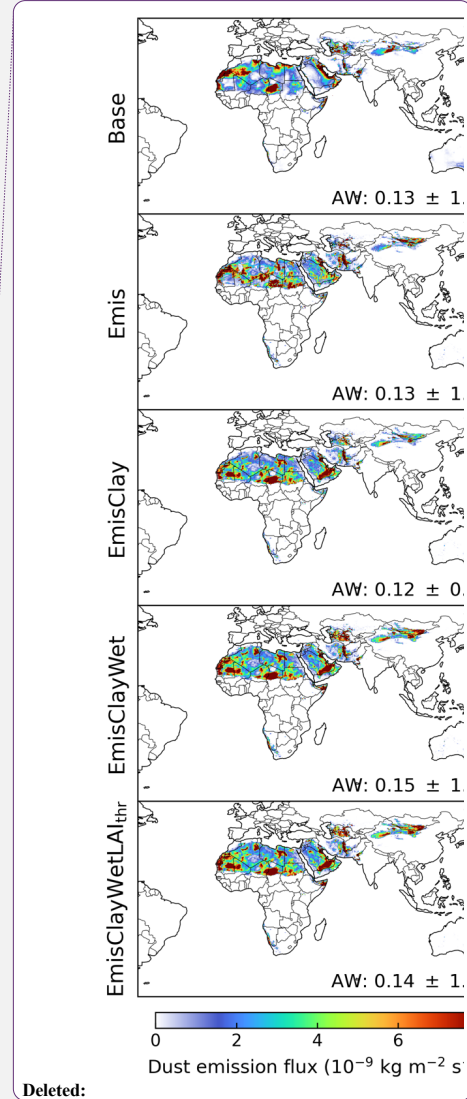
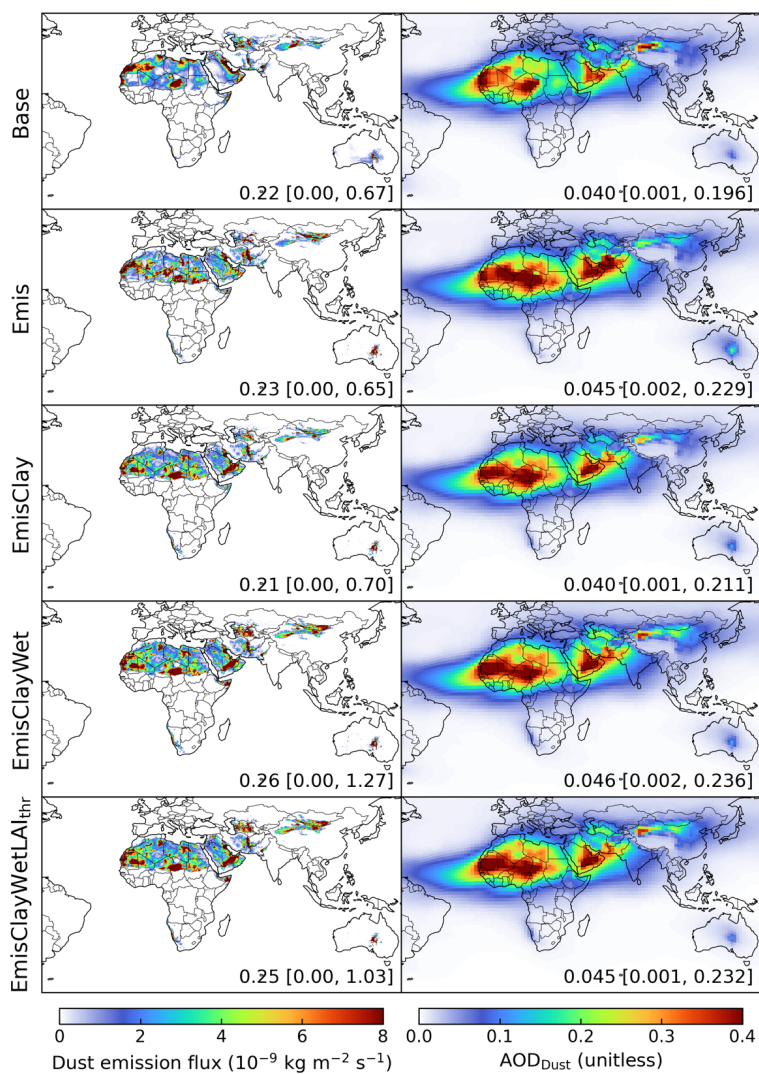
Deleted: .

Deleted: Figure 7

Deleted: 73% (Figure 2) to 37% (Figure 7

Deleted: Figure 6).

Field Code Changed



Deleted:

Deleted: Figure 4

Deleted: area-weighted (AW)

Deleted: standard deviation globally

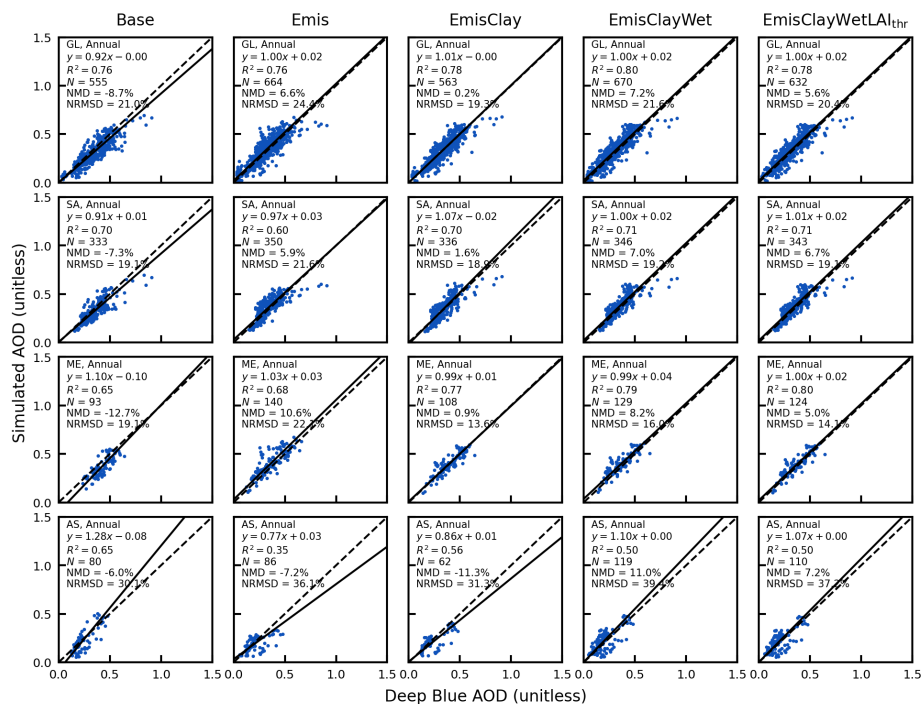


Figure 6. Comparisons of annual simulated aerosol optical depth (AOD) versus the Deep Blue satellite AOD globally (GL) and over main dust source regions of the Sahara – SA, Middle East – ME, and Asia (AS) with different emission schemes. Regression statistics including reduced-major-axis linear regression equation, coefficient of variation (R^2), total number of points (N), normalized mean difference (NMD), and normalized root-mean-square difference (NRMSD) are in the top left. [Note the total number of points varies across different schemes.](#)

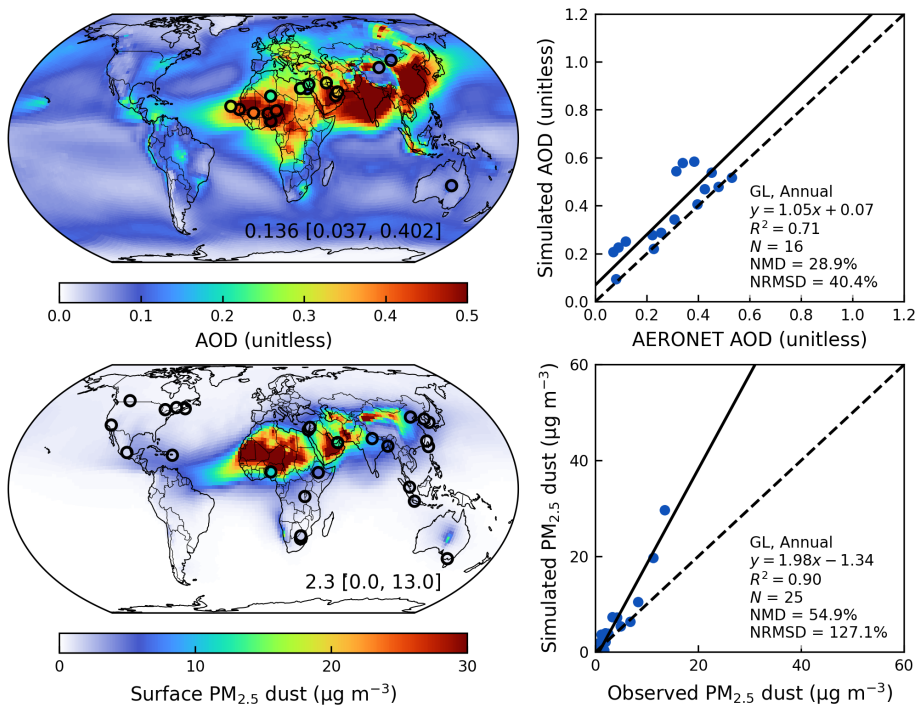
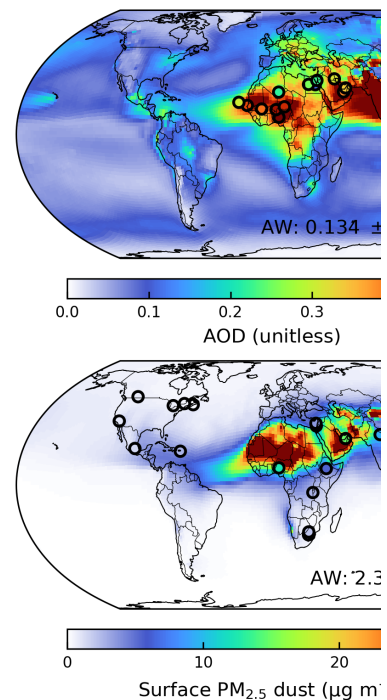


Figure 7. Annual simulated aerosol optical depth (AOD) and comparison against ground-based observations from the AERONET over dusty regions ($AOD_{Dust}/AOD > 0.5$) (top); Annual simulated surface $PM_{2.5}$ dust and comparison against ground-based measurements from the SPARTAN from the Emis* simulation in the year of 2018 (bottom). Filled circles on the maps represent ground-based observations from SPARTAN and AERONET. Inset values at the bottom right of the maps are arithmetical mean with 5th and 95th percentiles in the square brackets. Regression statistics including the reduced-major-axis linear regression equation, coefficient of variation (R^2), total number of points (N), normalized mean difference (NMD), and normalized root-mean-square difference (NRMSD) are listed at the bottom right of the scatter plots.

4.3 Improving the representation of fine mineral dust

As the size distribution of mineral dust is particularly important for the performance discrepancy between simulated AOD over dusty regions and surface $PM_{2.5}$ dust, we focus on improving its size-



Deleted:

Deleted: area-weighted (AW)

Deleted: standard deviation

613 resolved source and sink.

614 4.3.1 Revisiting the size distribution of emitted mineral dust

615 Figure 8a shows different PSDs including the default PSD used in the GEOS-Chem (GC PSD) based
616 on the brittle fragmentation theory with the side crack propagation length λ of 8 μm (Zhang et al.,
617 2013), the Kok PSD with λ of 12 μm (Kok, 2011), and the Meng PSD focusing on the optimization for
618 coarse to super coarse dust (Meng et al., 2022), in comparison with the observed PSD from the
619 2011 Fennec campaign (Ryder et al., 2013). While all modelled PSDs are within the wide range of
620 PSD from the Fennec campaign, the fraction of emitted DST1 from the Kok PSD exhibits greater
621 consistency with the Fennec observations than the other two PSDs. The larger discrepancy for the
622 size distribution with diameter less than $\sim 0.4 \mu\text{m}$ between the observed PSD from Fennec and
623 parametrized PSDs is possibly due to anthropogenic aerosol influence (González-Flórez et al.,
624 2023). In addition, a recent field study in the Moroccan Sahara (González-Flórez et al., 2023)
625 indicated overall agreement of emitted dust size distributions against the Kok PSD especially at the
626 fine diameter range. Therefore, we adopt the Kok PSD with λ of 12 μm for the size distribution of
627 emitted mineral dust in GEOS-Chem. Figure 8b shows the spatial distribution from the Emis*PSD
628 simulation which remains similar to that from the Emis* simulation in Figure 7. Reduced emissions
629 from DST1 by using the Kok PSD reduces the overestimation of surface $\text{PM}_{2.5}$ dust from 55% to 33%
630 compared to the ground-based measurements from SPARTAN (Figure 8c).

Deleted: Figure 8

Deleted: Larger

Formatted: Font: +Body (Aptos)

Formatted: Font: +Body (Aptos)

Formatted: Font: +Body (Aptos)

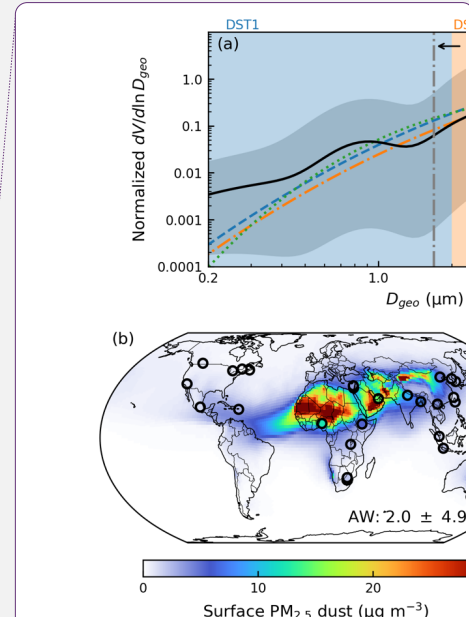
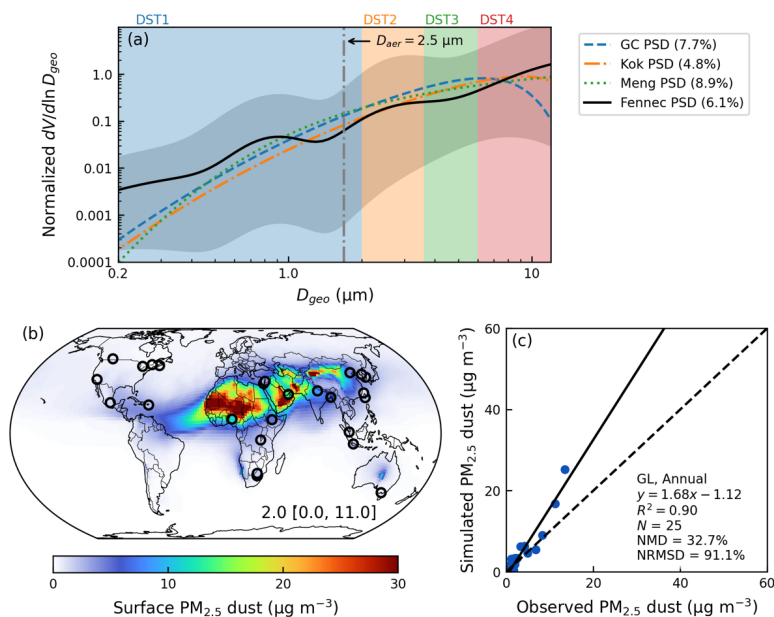
Deleted: Figure 8

Deleted: Figure 7.

Deleted: 37

Deleted: 17

Field Code Changed



Deleted: Grey

Deleted: area-weighted (AW)

Deleted: standard deviation

4.3.2 Improving the size-resolved dry and wet deposition of mineral dust

The default below-cloud (washout) scavenging of dust by rain and snow in GEOS-Chem is separated for fine (DST1) and coarse dust (DST2 to DST4) (Wang et al., 2011). However, washout scavenging coefficients strongly depend on aerosol size (Wang et al., 2014b). To improve the size-dependent washout treatment of dust, we update washout rates by rain and snow for 7 dust size bins by (Wang et al., 2014b):

$$\Lambda = A(D_d) \left(\frac{P_d}{f_r} \right)^{B(D_d)} \quad (9)$$

where Λ is the washout scavenging coefficient in s^{-1} by either rain or snow; P_d is the precipitation rate in mm h^{-1} falling from upper layers; f_r is the area fraction of precipitation within each grid box; A and B are empirical constants dependent on dust size D_d . Using the same semi-empirical equations for A and B as Wang et al. (2014b), the updated values for different dust size bins with different effective spherical radii are summarized in Table 2.

Table 2. Values of A and B for washout parametrizations by rain and snow for different dust size bins.

Diameter (μm)	Rain ($T \geq 268 \text{ K}$)		Snow ($248 \text{ K} \leq T < 268 \text{ K}$)	
	A	B	A	B
Bin1 (0.2–0.36)	4.0×10^{-7}	0.71	7.3×10^{-6}	0.57
Bin2 (0.36–0.6)	4.1×10^{-7}	0.71	1.3×10^{-5}	0.56
Bin3 (0.6–1.2)	4.8×10^{-7}	0.72	2.7×10^{-5}	0.56
Bin4 (1.2–2.0)	8.4×10^{-7}	0.73	6.0×10^{-5}	0.55
Bin5 (2.0–3.6)	4.8×10^{-5}	0.88	4.2×10^{-4}	0.61
Bin6 (3.6–6.0)	2.2×10^{-4}	0.87	1.3×10^{-3}	0.67
Bin7 (6.0–12.0)	3.4×10^{-4}	0.84	2.4×10^{-3}	0.73

Figure 9 shows the size-dependent variations of mineral dust dry and wet deposition. We adopt the effective radii for 7 dust size bins for dry and wet deposition. The dry deposition velocity can vary by a factor of 4.9 among Bin1 to Bin4 with the minimum near the geometric diameter of $0.5 \mu\text{m}$. The washout scavenging coefficient can vary by a factor of 2.6 among Bin1 to Bin4 with the minimum

Deleted: , varying by 3 orders of magnitude for diameter ranging from 1 to $10 \mu\text{m}$

Deleted: Figure 9

679 near the geometric diameter of 0.4 μm . Given the steep increasing strength of emitted dust from
 680 Bin1 to Bin4 (Figure 8), there is need to explicitly track dust within DST1. We evaluate these
 681 developments by examining their effects on the fractional contributions of fine dust to total dust.

Deleted: Figure 8

682 Figure 10 shows the fractional contributions of fine dust with geometric diameter less than 2 μm to
 683 total dust ($\text{AOD}_{\text{FineDust}}/\text{AOD}_{\text{Dust}}$) from the simulations with a total of 7 dust bins for dry deposition
 684 with updated washout scavenging parametrization and their differences. Due to the dominance of
 685 dry deposition over arid dusty regions, the explicit tracking of fine dust dry deposition slightly
 686 reduces $\text{AOD}_{\text{FineDust}}/\text{AOD}_{\text{Dust}}$ over major dust source regions. However, the anthropogenic
 687 contributions to fine dust are correspondingly enhanced over urban and industrial regions, leading
 688 to degraded comparison against SPARTAN measurements (Figure A5). We thus halve the AFCID
 689 emissions to reduce the excessive contributions from this uncertain source
 690 ($\text{Emis} \times \text{PSD7Bins0.5AD}$). In addition, accounting for the steep washout scavenging efficiency across
 691 DSTbin5 to DSTbin7 (Figure 9) with updated washout parametrization would induce enhanced
 692 fractional contributions especially for DSTbin5 (Figure A6) and thus relatively reduce fractional
 693 contributions from fine dust with geometric diameter less than 2 μm to total dust
 694 ($\text{AOD}_{\text{FineDust}}/\text{AOD}_{\text{Dust}}$). Figure 11 shows the overall performance with all revisions from the
 695 simulation of $\text{Emis} \times \text{PSD7Bins0.5ADWetDep}$. The reduced-major-axis linear regression slope is
 696 further reduced from 1.68 (Figure 8) to 1.59 with comparable values of NMD against SPARTAN
 697 measurements.

Deleted: Figure 10

Deleted: Figure A3).

Deleted: scale

Deleted: by half

Deleted: Figure 9

Deleted: Figure A4

Deleted: Figure 11

Deleted: 53

Deleted: Figure 8

Deleted: 44

698 Comparisons against other surface dust datasets also show improved or comparable performance
 699 compared to the Base simulation. Figure A7 shows the comparison against ground observations
 700 over North America. Using the refined new dust emission scheme with the replacement of the size
 701 distribution from the Kok PSD, explicitly tracking submicron bins for dry deposition, and updating
 702 the washout scavenging parametrization contribute to a comparable extent to reduce the
 703 overestimation over North America from 43% of the Base simulation to 15% of the
 704 $\text{Emis} \times \text{PSD7Bins0.5ADWetDep}$ simulation. Comparisons against surface concentrations and total
 705 deposition of PM_{10} dust (Li et al., 2022b) for the $\text{Emis} \times \text{PSD7Bins0.5ADWetDep}$ simulation are also
 706 comparable with the Base simulation (Figures A8 and A9). Consistent with prior studies about the
 707 spatial sensitivity of dust emissions (Leung et al., 2023; Meng et al., 2021), fine-resolution
 708 meteorological fields are needed to capture dust emission hotspots. If the dust emissions were
 709 calculated with C48 meteorological fields, the global dust distribution would become more

Deleted: Figure A5

Deleted: -

Deleted: explicitly

Deleted: A6

Deleted: A7

Deleted: The simulated total column AOD would be underestimated by 14% compared to AERONET, and the surface fine dust would be underestimated by 22% compared to SPARTAN if...

Deleted: are

Deleted: at C48 resolution

concentrated in the major global source regions with the elimination of marginal dust sources, and the R^2 versus SPARTAN surface $PM_{2.5}$ dust would diminish to 0.83 (Figure A10). Overall comparisons for the seasonal mean between the Base and the Emis*PSD7Bins0.5ADWetDep simulations confirm largely reduced overestimation for the surface fine dust against SPARTAN, while retaining comparable skill for the total column AOD against AERONET (Figures A11 to A14). The reduction of surface overestimation is especially prominent over dusty seasons in Spring (from 73% to 48%) and Summer (from 138% to 50%), while further improvements are needed for surface overestimation in Fall (from 140% to 95%).

Table 3 summarizes the effects of different modifications on the model performance of total column AOD and surface fine mineral dust in this study. Strong overestimation of surface $PM_{2.5}$ dust concentrations exist in the Base simulation by a factor of 2.4 versus SPARTAN measured dust. Updating the dust emission scheme with further refinements in the soil properties reduces the overestimation of surface $PM_{2.5}$ dust by 39%. The surface overestimation by 55% is reduced to 35% by updating the size distribution of emitted dust, explicitly tracking dust with diameter less than 2 μm in 4 bins, and updating the parametrization of below-cloud scavenging. The comparisons of simulated AOD versus AERONET and Deep Blue AOD are comparable for all simulations with the correlation coefficient of 0.8-0.9, and NMDs from -9% to 31%. The emissions between the Base and Emis* simulations are comparable with the global annual dust emission of $\sim 2000 \text{ Tg yr}^{-1}$, which is within the range of 1000-5000 Tg yr^{-1} from intercomparison projects (Huneeus et al., 2011; Wu et al., 2020). As the Kok PSD reduces the mass fraction of fine dust, the total emitted mass is enhanced to $\sim 3000 \text{ Tg yr}^{-1}$ with larger contributions from coarse dust. The reduction of surface $PM_{2.5}$ dust overestimation with these revisions is confirmed if SPARTAN sites are restricted to those with at least 50 samples as well (Table A3).

Deleted: A9 to A12).

Deleted: Table 3

Deleted: 2

Deleted: 36

Deleted: 37

Deleted: 21

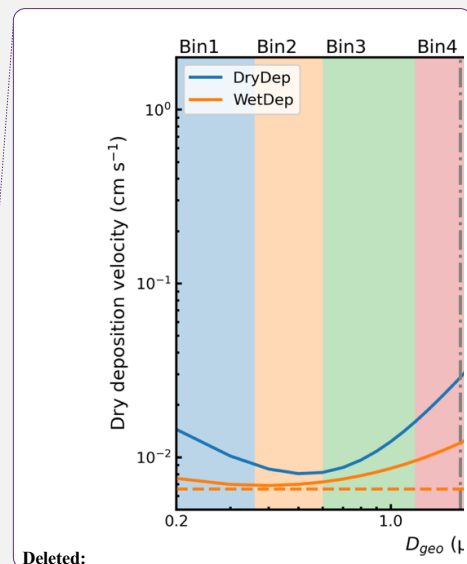
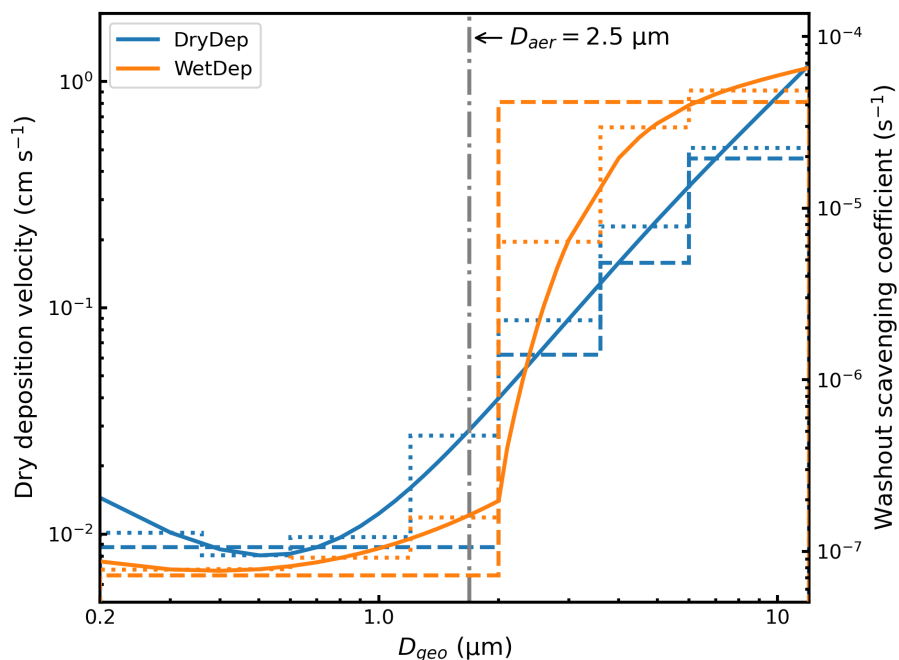


Figure 9. Size-resolved dry deposition velocity over desert (left y-axis) and washout scavenging coefficient by rain (right y-axis). Dry deposition velocity is calculated with the friction velocity of 0.4 m s^{-1} and the particle density of 2500 kg m^{-3} with the default dry deposition scheme used in the GEOS-Chem. Washout scavenging coefficient is calculated with the precipitation rate of 0.1 mm h^{-1} with the updated washout parametrization. Solid lines indicate theoretical parametrization. Dashed lines indicate the default discrete treatment. Dotted lines indicate the updated discrete treatment. Grey dash-dotted line indicates the corresponding geometric diameter of $1.7 \mu\text{m}$ for the aerodynamic diameter of $2.5 \mu\text{m}$.

Deleted: Orange horizontal dash

Deleted: washout scavenging coefficients by rain with

Deleted: precipitation rate of 0.1 mm h^{-1} for fine aerosol (Bin1 to Bin4) and coarse aerosol (Bin5 to Bin7).

Deleted: Filled rectangles indicate different simulated dust size bins.

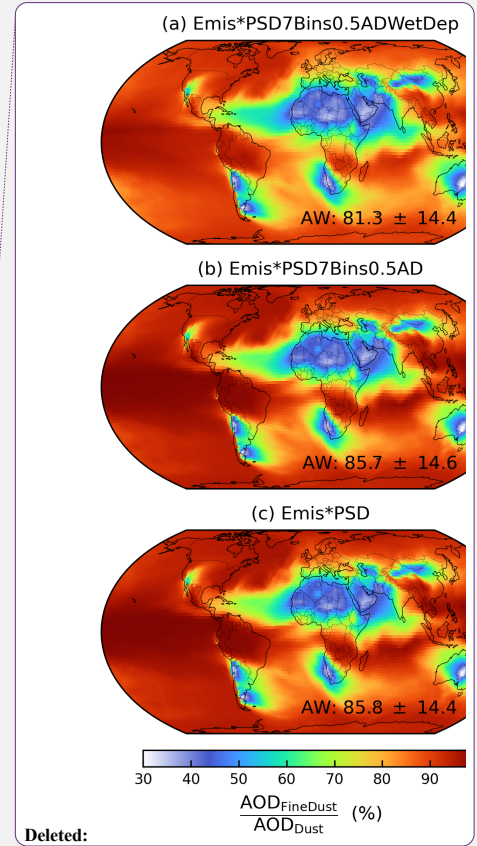
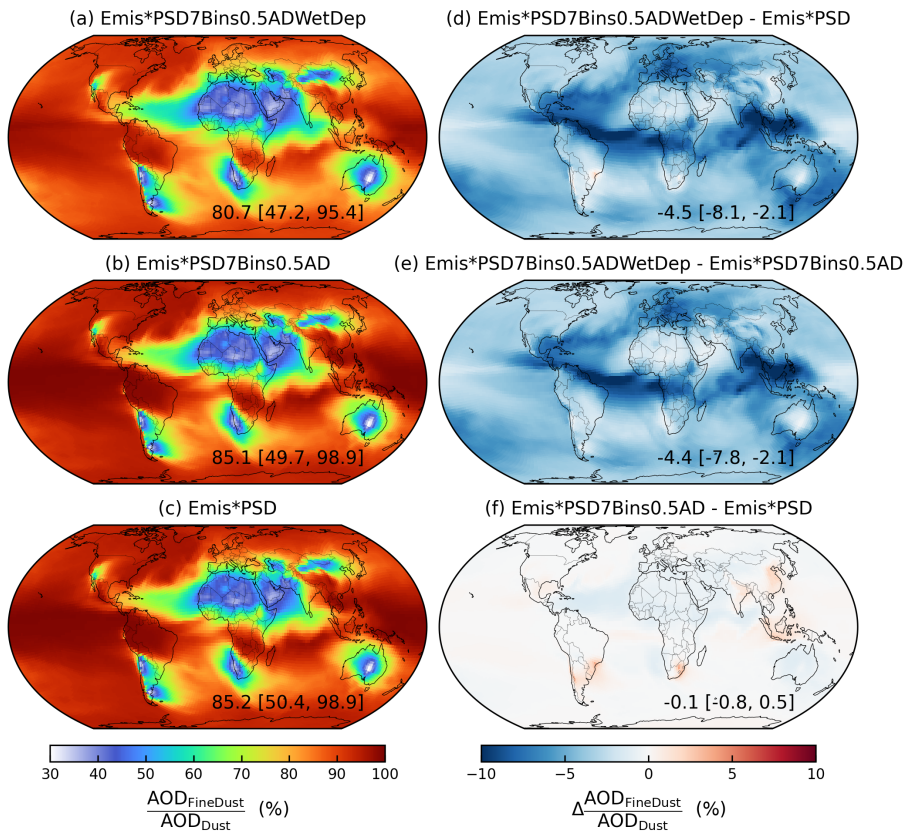


Figure 10. Fractional contributions of fine dust with geometric diameter less than $2 \mu m$ to total dust column abundance ($AOD_{FineDust}/AOD_{Dust}$) from the a) Emis*PSD7Bins0.5ADWetDep, b) Emis*PSD7Bins0.5AD, c) Emis*PSD and their absolute differences. Inset values at the bottom right are arithmetical mean with 5th and 95th percentiles in the square brackets.

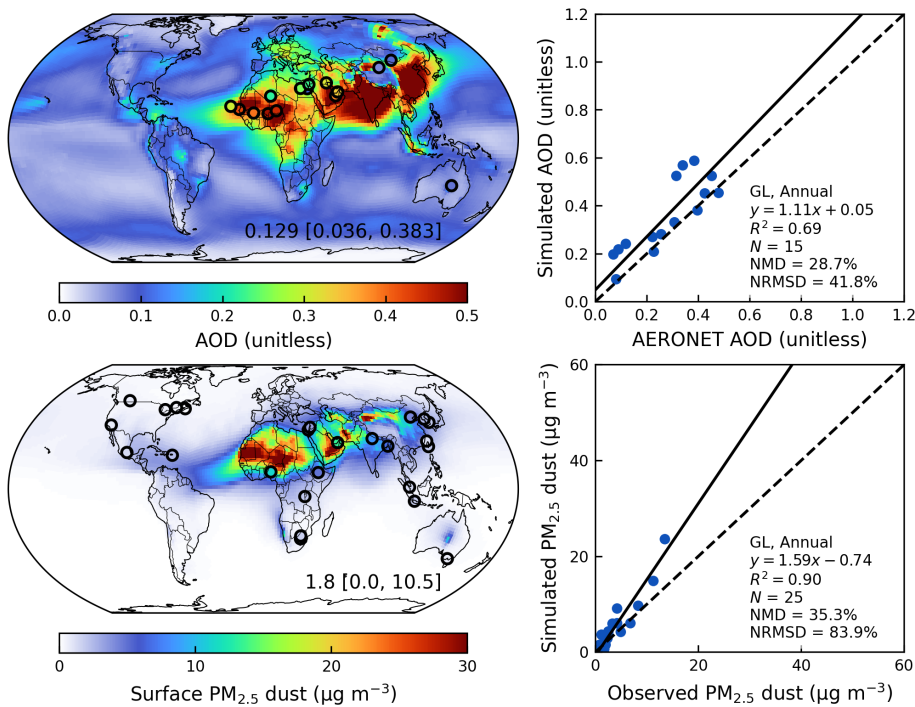
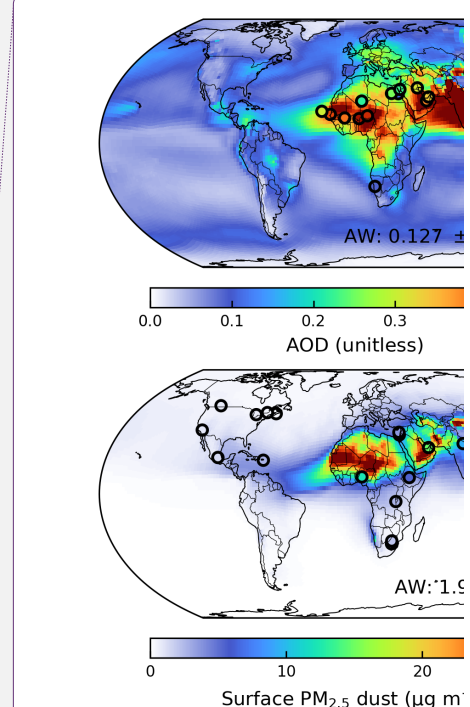


Figure 11. Annual simulated aerosol optical depth (AOD) and comparison against ground-based observations from AERONET over dusty regions ($AOD_{Dust}/AOD > 0.5$) (top); Annual simulated surface PM_{2.5} dust and comparison against ground-based measurements from SPARTAN from the Emis*PSD7Bins0.5ADWetDep simulation in the year of 2018 (bottom). Filled circles on the maps represent ground-based observations from SPARTAN and AERONET. Inset values at the bottom right of the maps are arithmetic mean with 5th and 95th percentiles in the square brackets. Regression statistics including the reduced-major-axis linear regression equation, R^2 , total number of points (N), normalized mean difference (NMD), and normalized root-mean-square difference (NRMSD) are listed at the bottom right of the scatter plots.



Deleted:

Deleted: area-weighted (AW)

Deleted: standard deviation

Deleted: ¶

Deleted: total ...nnual dust optical depth (AOD_{Dust}) and

Deleted: 95...6

Deleted: 20...2

Deleted: 79...6

Deleted: 69...5

Deleted: 94...5

Deleted: 80...8

Deleted: 53...8

Deleted: 94...5

Deleted: 48...3

Deleted: 44...9

Deleted: total ...nnual dust optical depth (AOD _{Dust}) and
Deleted: 95...6
Deleted: 20...2
Deleted: 79...6
Deleted: 69...5
Deleted: 94...5
Deleted: 80...8
Deleted: 53...8
Deleted: 94...5
Deleted: 48...3
Deleted: 44...9

845 5 Conclusions

846 In summary, we evaluate and improve the [annual](#) mineral dust simulation in the GEOS-Chem
847 model by building upon recent ground-based measurements from SPARTAN of mineral dust in
848 PM_{2.5} over land, together with total column AOD from AERONET measurements and from [the](#)
849 MODIS and VIIRS Deep Blue satellite [products](#). We devote attention to the representation of
850 aerodynamic diameter when comparing with ground-based PM_{2.5} measurements, since
851 representation as geometric diameter in models would introduce [a](#) two-fold bias. We nonetheless
852 find that the standard GEOS-Chem chemical transport model much better represents columnar
853 AOD with a slope near unity than surface PM_{2.5} dust concentrations which are overestimated by a
854 factor of two. Comparison of simulated extinction [profiles](#) versus the 15-year climatological
855 CALIOP extinction [profiles](#) yields overall consistency in the vertical shape (Figure 3), indicating the
856 importance of other dominant factors.

857 We develop the mineral dust representation in GEOS-Chem with attention to its sources, size
858 distribution, and sinks. We implement a new dust emission scheme based on Leung et al. (2023)
859 with further refinements to the clay content and wetness in the topsoil layer, threshold leaf area
860 index, and reducing dust emissions over snow and vegetation covered land surfaces. The NMD
861 versus surface measurements is reduced by [39%](#) while the simulated AOD better represents the
862 spatial distribution of Deep Blue AOD over dusty regions. To further improve the fine dust
863 representation in GEOS-Chem, we revisit the size distribution of emitted dust and find [that](#) the Kok
864 particle size distribution (PSD; Kok, 2011) better represents the mass fraction of fine dust
865 measured during the Fennec field campaign over Northern Africa than [does](#) the default PSD
866 [despite the uncertainties from the Fennec observations. The](#) implementation [of the Kok PSD](#) into
867 GEOS-Chem reduces the surface overestimation of PM_{2.5} dust by [22%](#). We also enable explicit
868 tracking of mineral dust with geometric diameter less than 2 µm in 4 size bins for emission,
869 transport, and deposition with updated parametrization for below-cloud scavenging, which further
870 reduces the overestimation of surface PM_{2.5} dust concentrations to within [35%](#).

871 [Despite these advances, challenges remain in mineral dust development and evaluation. The](#)
872 [performance of AOD against satellite and AERONET observations over dusty regions may still be](#)
873 [affected by other aerosol components which may benefit from further evaluations and](#)
874 [developments. Although the simulations are only for a single year, we average the multi-year](#)

Deleted: product

Deleted: profile

Deleted: profile

Deleted: Figure 3

Deleted: 36

Deleted: and that its

Deleted: 20

Deleted: 21

observational data from the CALIOP extinction profile and SPARTAN measured surface dust concentrations for long-term representativeness. This approach benefits from the weak interannual variability of annual mean mineral dust concentrations (Li et al., 2017; Song et al., 2021). Nonetheless, additional observational data will enable further evaluation of the performance of mineral dust simulations. In addition, knowledge gaps remain for mechanistic representation of mineral dust emissions. We call for further developments on the parametrization of dust emissions, particularly for the uncertainties in global and regional dust emission strength and further constraints on the effects of soil wetness on the threshold friction velocity. Future examination of daily variability would also be valuable for short-term predictability.

These investigations indicate the importance of size type reconciliation in models versus measurements, the spatial distribution of dust emissions, the size distribution of emitted dust, and the explicit tracking of fine dust bins for more accurate simulation of fine dust abundance from the surface to the column.

Appendix A: Additional details about dust emission parametrizations, SPARTAN dust, and complementary figures

A1. A global dust equation

We follow a global dust equation for the calculation of surface PM_{2.5} dust concentrations from SPARTAN (Liu et al., 2022):

$$\text{Dust} = [1.89\text{Al} \times (1 + \text{MAL}) + 2.14\text{Si} + 1.40\text{Ca} + 1.36\text{Fe} + 1.67\text{Ti}] \times \text{CF} \quad (\text{A1})$$

where 1.89, 2.14, 1.40, 1.36, and 1.67 are the mass conversion ratios for corresponding mineral oxides; MAL is the mineral-to-aluminum mass ratio of (K₂O + MgO + Na₂O)/Al₂O₃; CF is a correction factor (CF) to account for other missing compounds.

A2. Horizontal saltation flux in standard version of GEOS-Chem

The default horizontal saltation flux Q_s in GEOS-Chem is based on the parametrization of White (1979):

$$Q_s = C_z \frac{\rho_a}{g} u_{*s}^3 \left(1 - \frac{u_{*ft}}{u_{*s}}\right) \left(1 + \frac{u_{*ft}}{u_{*s}}\right)^2 \text{ for } u_{*s} > u_{*ft} \quad (\text{A2})$$

909 where $C_z = 2.61$ is the saltation constant; ρ_a is the air density in kg m^{-3} ; $g = 9.81 \text{ m s}^{-2}$ is the
 910 gravitational acceleration; the drag partitioning effects are ignored by default and thus $u_{*s} = u_*$,
 911 where u_* is calculated from the wind speed at 10 m u_{10m} based on the logarithmic wind profile
 912 within the boundary layer under adiabatic conditions (Marticorena and Bergametti, 1995):

$$913 \quad u_* = \frac{ku_{10m}}{\ln(z_0/z_{0a})} \quad (A3)$$

914 where $k = 0.4$ is the von Kármán constant; u_{10m} is the wind speed at 10 m; $z_0 = 10 \text{ m}$ is the
 915 reference height; $z_{0a} = 10^{-4} \text{ m}$ is the surface roughness height. The wet fluid threshold friction
 916 velocity of u_{*ft} is the minimum surface friction velocity required to initiate the saltation from the
 917 bare soil (Fécan et al., 1999):

$$918 \quad u_{*ft} = u_{*ft0} \cdot f_m \quad (A4)$$

919 where u_{*ft0} is the dry fluid threshold friction velocity following Iversen and White (1982):

$$920 \quad u_{*ft0} = \begin{cases} \frac{0.129K}{\sqrt{1.928Re^{0.092} - 1}}, & 0.03 < Re < 10 \\ 0.12K[1 - 0.0858e^{-0.0617(Re-10)}], & Re \geq 10 \end{cases} \quad (A5)$$

921 where:

$$922 \quad K = \sqrt{\frac{\rho_p g D_p}{\rho_a} \left(1 + \frac{0.006}{\rho_p g D_p^{2.5}} \right)} \quad (A6)$$

$$923 \quad Re = 1331D_p^{1.56} + 0.38 \quad (A7)$$

924 Where $D_p = 75 \text{ }\mu\text{m}$ is the diameter of soil particle which corresponds to the minimum dry fluid
 925 threshold velocity of u_{*ft0} (Iversen and White, 1982).

926 The enhancement factor $f_m \geq 1$ is a function of soil wetness (Fécan et al., 1999):

$$927 \quad f_m = \begin{cases} 1, & w \leq w_t \\ \sqrt{1 + 1.21[100(w - w_t)]^{0.68}}, & w > w_t \end{cases} \quad (A8)$$

928 where w is the gravimetric soil moisture (kg kg^{-1}) in the shallowest soil layer; w_t is the threshold

929 gravimetric water content above which u_{*ft} increases with soil wetness (Fécan et al., 1999):

$$930 \quad w_t = 0.01a (17f_{clay} + 14f_{clay}^2) \quad (A9)$$

931 where a is a tuning factor which is taken as $1/f_{clay} = 5$ by default.

932 **A3. Additional details about the new dust emission scheme**

933 The variables used in the calculation for the total dust emission flux F_d (Equation (6)) can be
 934 categorized into meteorological fields including η , ρ_a , and u_* , land surface properties including
 935 f_{bare} , f'_{clay} , F_{eff} , and u_{*it} , intrinsic soil erodibility properties including u_{*st} , C_d , and κ , and a global
 936 tuning factor of C_{tune} .

937 Intermittency effects due to the fluctuation of instantaneous soil friction velocity u_s are reflected in
 938 the intermittency factor of η , which is denoted by the temporal fraction of active dust emission
 939 ranging from 0 to 1 within a transport time step. The parametrization of η is based on Comola et al.
 940 (2019):

$$941 \quad \eta = 1 - P_{ft} + \alpha(P_{ft} - P_{it}) \quad (A10)$$

942 where P_{ft} and P_{it} are the cumulative probability of instantaneous friction velocity larger than a wet
 943 fluid threshold, and an impact threshold, respectively; α is the fraction of u_s crossing a wet fluid
 944 threshold over the total fraction crossing a wet fluid threshold and an impact threshold.

945 The calculation of η is based on velocity at the saltation height of $z_{sal} = 0.1$ m. Thus the surface
 946 friction velocity of u_{*s} , and threshold velocities of u_{*ft} and u_{*it} are first calculated at the saltation
 947 height based on (Marticorena and Bergametti, 1995):

$$948 \quad u_X(sal) = \frac{u_{*X}}{k} \ln \left(\frac{z_{sal}}{z_{0a}} \right) \quad (A11)$$

949 where the subscript X can be ft , it or s , $z_{0a} = 10^{-4}$ m, and $k = 0.386$ is the von Kármán constant.

950 Assuming a normal distribution of instantaneous soil friction velocity $u_s \sim N(u_s, \sigma_{u_s}^2)$, a standard
 951 deviation of instantaneous friction velocity σ_{u_s} is a central parameter to calculate the fraction of
 952 active dust emissions within a time step for transportation. σ_{u_s} is calculated based on the similarity

theory (Panofsky et al., 1977):

$$\sigma_{u_s} = u_{*s} \left(12 - 0.5 \frac{z_i}{L} \right)^{1/3} \quad (A12)$$

where z_i is the planetary boundary layer height, and L is the Monin-bukhov length calculated by (Panofsky et al., 1977):

$$L = - \frac{\rho_a c_p T u_s^3}{kgH} \quad (A13)$$

where $c_p = 1005 \text{ J kg}^{-1} \text{ K}^{-1}$ is the specific heat capacity of air under constant pressure; T is surface air temperature; u_s in m s^{-1} is the original surface friction velocity without the drag partitioning correction; $g = 9.81 \text{ m s}^{-2}$ is the gravitational acceleration; H is the sensible heat flux from turbulence in W m^{-2} .

Given that a normal distribution is assumed, cumulative probabilities of P_{ft} and P_{it} can be calculated by $P_{ft} = 0.5[1 + \text{erf}(\frac{u_{ft}-u_s}{\sqrt{2}\sigma_{u_s}})]$, and $P_{it} = 0.5[1 + \text{erf}(\frac{u_{it}-u_s}{\sqrt{2}\sigma_{u_s}})]$. α is the number of crossing rate of u_s across the wet fluid threshold C_{ft} over the total number of crossing rate of u_s across the wet fluid threshold C_{ft} and the impact threshold C_{it} (Comola et al., 2019):

$$\alpha = \frac{C_{ft}}{C_{ft} + C_{it}} \quad (A14)$$

The crossing fraction of α is approximated by $\alpha \approx [\exp(\frac{u_{ft}^2 - u_{it}^2 - 2u_s(u_{ft} - u_{it})}{2\sigma_{u_s}^2}) + 1]^{-1}$ as suggested by Comola et al. (2019).

The soil surface friction velocity of u_{*s} is calculated by (Leung et al., 2023; Marticorena and Bergametti, 1995; Webb et al., 2020):

$$u_{*s} = u_* F_{eff} \quad (A15)$$

where u_* is the surface friction velocity taken directly from the parent meteorological fields; F_{eff} is the drag partitioning effects due to the presence of non-erodible elements including rocks and vegetation.

975 Drag partitioning effects are calculated following Leung et al. (2023):

$$976 \quad F_{eff} = (A_r f_{eff,r}^3 + A_v f_{eff,v}^3)^{1/3} \quad (A16)$$

977 where A_r is the fraction of barren and sparsely vegetated land cover approximated by A_{erod} ; A_v is
 978 the fraction of short vegetation land cover taken from the MCD12C1 Version 6.1 land cover
 979 product; $f_{eff,r}$ is the drag partitioning effects due to rocks (Marticorena and Bergametti, 1995):

$$980 \quad f_{eff,r} = 1 - \frac{\ln\left(\frac{z_{0a}}{z_{0s}}\right)}{\ln\left[b_1 \left(\frac{X}{z_{0s}}\right)^{b_2}\right]} \quad (A17)$$

981 where z_{0a} is the aeolian roughness length which the surface roughness of overlaying nonerodable
 982 elements and was taken as the minimum of monthly mean gridded aeolian roughness length
 983 (Prigent et al., 2005); $z_{0s} = \frac{D_p}{15}$ is the smooth roughness length which quantifies the roughness of a
 984 bed of fine soil particles in the absence of roughness elements (Pierre et al., 2014b); $b_1 = 0.7$, $b_2 =$
 985 0.8 , and $X = 10$ m are empirical constants (Leung et al., 2023). $f_{eff,v}$ is the drag partitioning effects
 986 due to vegetation (Pierre et al., 2014a):

$$987 \quad f_{eff,v} = \frac{K + f_0 c}{K + c} \quad (A18)$$

988 where $f_0 = 0.32$ and $c = 4.8$ are empirical constants (Okin, 2008); K is calculated by $\frac{\pi}{2} \left(\frac{1}{LAI/LAI_{thr}} - \right.$
 989 $1) (Leung et al., 2023; Okin, 2008).$

990 The wet fluid threshold velocity u_{*ft} is calculated using Equation (A4), except the dry fluid threshold
 991 velocity u_{*ft0} is calculated by (Shao and Lu, 2000):

$$992 \quad u_{*ft0} = \sqrt{A(\rho_p g D_p + \gamma / D_p) / \rho_a} \quad (A19)$$

993 where $A = 0.0123$ and $\gamma = 1.65 \times 10^{-4} \text{ kg s}^{-2}$ are empirical constants (Darmenova et al., 2009;
 994 Leung et al., 2023); $D_p = 127 \pm 47 \text{ } \mu\text{m}$ is the median diameter of soil particle as evaluated from
 995 various field measurements in Leung et al. (2023).

996 Once the saltation is initialized, the threshold velocity required to maintain the saltation

diminishes, which is defined as the dynamic or impact threshold friction velocity u_{*it} in m s^{-1} (Martin and Kok, 2018):

$$u_{*it} = B_{it} u_{*ft0} \quad (\text{A20})$$

where $B_{it} = 0.82$. A prior study suggested that the impact threshold primarily governed the saltation flux (Martin and Kok, 2018) and thus u_{*it} is adopted as the governing threshold in Equation (14).

The standardized wet fluid threshold friction velocity u_{*st} was proposed and argued as a central factor to characterize soil aridity by a prior study (Kok et al., 2014):

$$u_{*st} = u_{*ft} \sqrt{\rho_a / \rho_{a0}} \quad (\text{A21})$$

where $\rho_{a0} = 1.225 \text{ kg m}^{-3}$ is the standard surface air density.

The fragmentation exponent of κ quantifies the sensitivity of F_d to u_{*s} and is capped at 3 to prevent excessive sensitivity of the model to wind speeds according to (Kok et al., 2014; Leung et al., 2024):

$$\kappa = C_\kappa \frac{(u_{*st} - u_{*st0})}{u_{*st0}} \quad (\text{A22})$$

where $C_\kappa = 2.7 \pm 1.0$ and $u_{*st0} = 0.16 \text{ m s}^{-1}$ are constants.

The time-varying soil erodibility coefficient is a function of u_{*st} only (Kok et al., 2014):

$$C_d = C_{d0} \exp\left(-C_e \frac{u_{*st} - u_{*st0}}{u_{*st0}}\right) \quad (\text{A23})$$

where $C_{d0} = (4.4 \pm 0.5) \times 10^{-5}$ and $C_e = 2.0 \pm 0.3$ are empirical constants.

1014

1015 Table A1. The mean and standard deviation (σ) of surface PM_{2.5} dust measured from 25 SPARTAN
 1016 sites with at least 10 samples in 5 years from 2019 to 2023 globally. Sites are sorted by the mean
 1017 surface PM_{2.5} dust concentrations.

Site	# of sample	Sampling days ^a	Sampling seasons	Start date for MAIA sites	Mean ($\mu\text{g m}^{-3}$)	σ ($\mu\text{g m}^{-3}$)
Abu Dhabi	113	1012	MAM, JJA, SON	-	13.4	6.7
Ilorin	47	411	MAM, JJA, SON	-	11.2	15.6
Kanpur	15	135	MAM, JJA, SON	-	8.2	7.3
Dhaka	49	170	MAM, JJA, SON	-	6.8	3.5
Addis Ababa	117	234	MAM, JJA, SON	12/7/2022	4.9	1.6
Beijing	83	424	MAM, JJA, SON	8/30/2022	4.2	2.0
Rehovot	181	571	MAM, JJA, SON	11/5/2021	4.2	4.0
Haifa	142	284	MAM, JJA, SON	2/16/2022	3.3	3.4
Seoul	83	744	MAM, JJA, SON	-	2.5	1.5
Fajardo	52	453	MAM, JJA, SON	-	2.3	2.3
Bujumbura	19	171	MAM, JJA, SON	-	2.0	1.2
Kaohsiung	122	244	MAM, JJA, SON	8/20/2022	1.9	0.8
Ulsan	77	682	MAM, JJA, SON	-	1.9	1.3
Pretoria	223	450	JJA, SON	4/15/2021	1.7	0.6
Bandung	28	249	MAM, JJA, SON	-	1.7	0.5
Singapore	13	117	JJA, SON, DJF	-	1.3	0.4
Johannesbur	166	331	MAM, JJA, SON	4/7/2022	1.3	0.3
Mexico City	49	425	MAM, JJA, SON	-	1.3	0.5
Taipei	211	421	MAM, JJA, SON	1/27/2022	1.1	0.9
Pasadena	242	484	MAM, JJA, SON	11/9/2021	0.8	0.3
Lethbridge	13	121	MAM, JJA, SON	-	0.7	0.3
Melbourne	34	307	MAM, JJA	-	0.6	0.8
Downsview	18	144	MAM, JJA, SON	-	0.5	0.2
Sherbrooke	83	687	MAM, JJA, DJF	-	0.4	0.2
Halifax	116	801	MAM, JJA, SON	-	0.3	0.1

1018 ^aThe number of days when SPARTAN sampling occurred for a part of the day according to either the
 1019 standard 9-day protocol or the MAIA protocol.

Deleted: , median,
 Deleted: 26
 Deleted: Latitude (°N)
 Deleted: Longitude (°E)
 Deleted: Mean ($\mu\text{g m}^{-3}$)
 Deleted: Median
 Deleted: Standard deviation
 Deleted: # of samples
 Formatted ... [1]
 Deleted: 136
 Deleted: 24.4
 Deleted: 54.6
 Deleted: 14.8
 Deleted: 14.1
 Deleted: .4
 Deleted: 58
 Deleted: 8.5
 Deleted: 4.7
 Deleted: 12.2
 Deleted: 7.1
 Deleted: 17.1
 Deleted: 18
 Deleted: 26.5
 Deleted: 80.2
 Deleted: 9.3
 Deleted: 6
 Deleted: 8.2
 Deleted: 23.7
 Deleted: 90.4
 Deleted: 53
 Deleted: 7.7
 Deleted: 7.4
 Deleted: 4.1
 Deleted: 113
 Deleted: 9.0
 Deleted: 38.8
 Deleted: 5.4
 Deleted: 5.0
 Deleted: 7
 Deleted: 169
 Deleted: 40.0
 Deleted: 116.3
 Deleted: 4.6
 Deleted: 3.9
 Deleted: 3
 Deleted: 183
 Deleted: 31.9
 Deleted: 34.8
 Deleted: 4.4
 Deleted: 3
 Deleted: 4
 Deleted: Hanoi ... [2]
 Deleted: 141
 Deleted: 32.8
 Deleted: 35.0
 Deleted: 3.6

1325 Table A2. The values of a global tuning factor C_{tune} used for different simulations.

Simulation	C_{tune}
Emis*	
Emis	2.358×10^{-2}
EmisClay	2.569×10^{-3}
EmisClayWet	2.146×10^{-3}
EmisClayWetLAI _{thr}	2.170×10^{-3}
Emis*PSD	2.945×10^{-3}
Emis*PSD7Bins0.5AD	2.892×10^{-3}
Emis*PSD7Bins0.5ADWetDep	2.832×10^{-3}

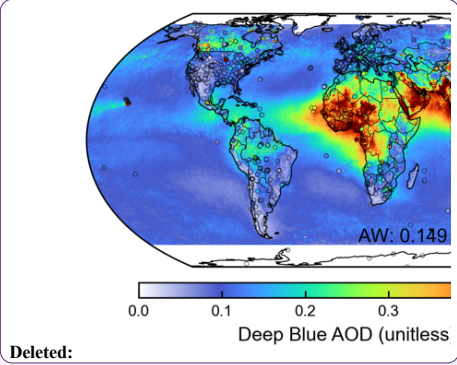
1326

1327 Table A3. Effects of different modifications on the model performance of simulated annual surface
1328 $PM_{2.5}$ dust versus SPARTAN over sites with >50 samples in terms of the correlation coefficient (r),
1329 the reduced-major-axis linear regression slope, and the normalized mean difference (NMD).

Simulation	Simulated surface $PM_{2.5}$ dust versus SPARTAN		
	r	slope	NMD (%)
Base	0.96	2.71	115.8
Emis*			
Emis	0.97	2.24	87.1
EmisClay	0.97	2.01	45.7
EmisClayWet	0.97	2.30	89.8
EmisClayWetLAI _{thr}	0.97	2.23	78.7
Emis*PSD	0.97	1.90	53.1
Emis*PSD7Bins0.5AD	0.96	1.85	64.6
Emis*PSD7Bins0.5ADWetDep	0.97	1.80	58.2

1330

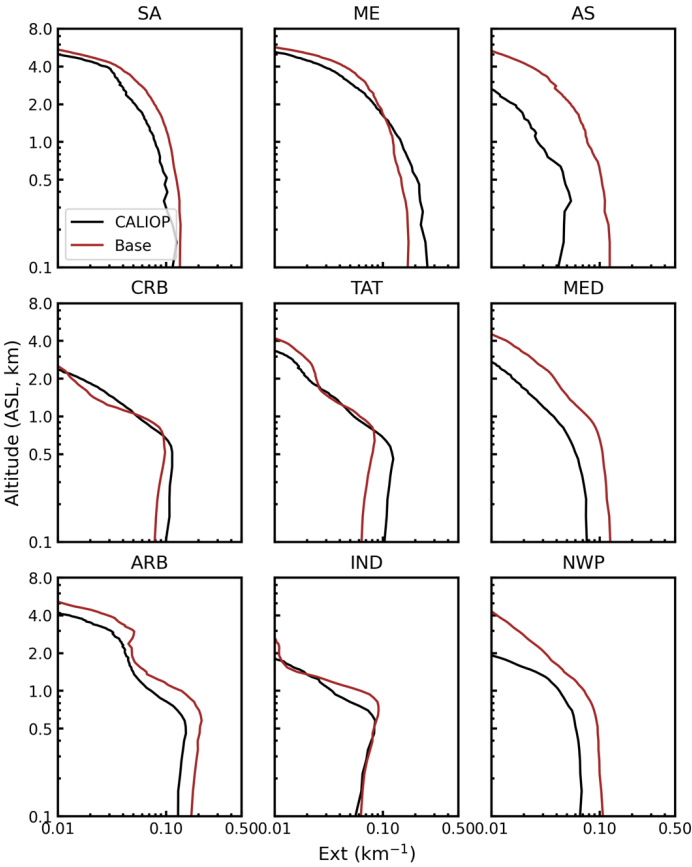
1331



1333 Table A4. Computational demand of 4-bin and 7-bin dust simulations

Type	Number of physical cores (CPUs) ^a	Throughput (d d ⁻¹)
4 dust bins	108	78.9
7 dust bins		74.2

1334 ^aCalculated on Intel® Xeon® Gold 6154 with the clock speed of 3.00 GHz.



1335
1336 Figure A1. Same as Figure 3 but for the absolute extinction vertical profile.

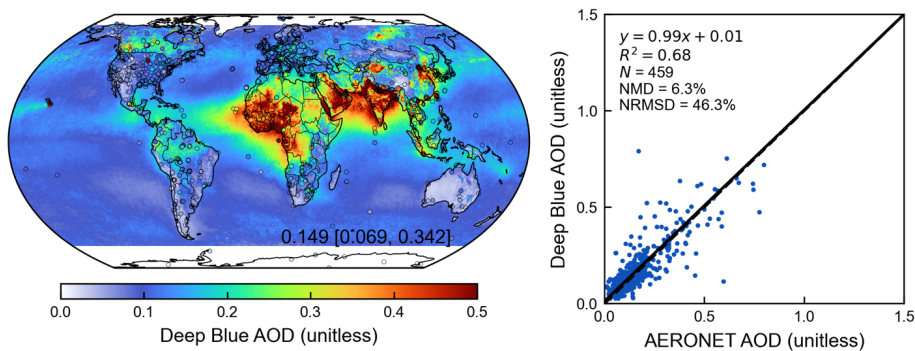
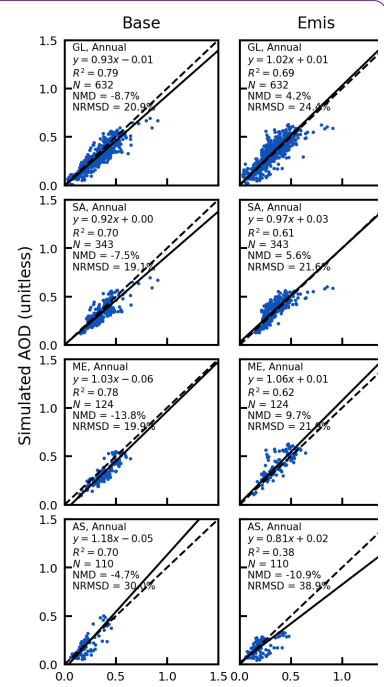
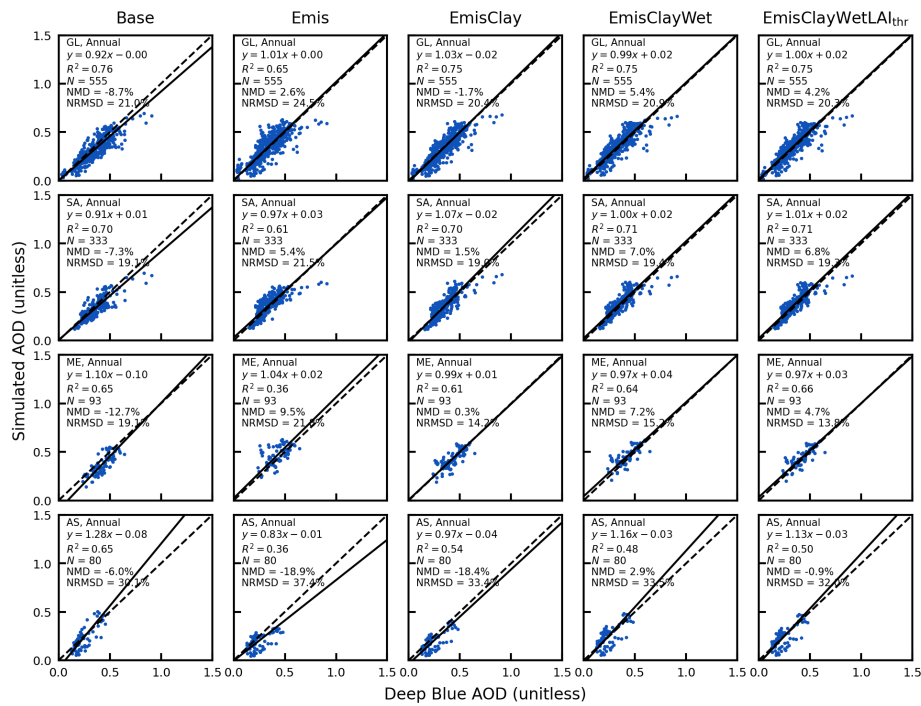


Figure A2. Annual aerosol optical depth (AOD) from the Deep Blue satellite retrieval and comparison against ground-based observations from AERONET in the year of 2018. Filled circles on the map represent ground-based observations from AERONET. Inset values at the bottom right of the map are arithmetical mean with 5th and 95th percentiles in the square brackets. Regression statistics including the reduced-major-axis linear regression equation, coefficient of variation (R^2), total number of points (N), normalized mean difference (NMD), and normalized root-mean-square difference (NRMSD) are listed at the top left of the scatter plot.

Deleted: area-weighted (AW)

Deleted: standard deviation



Deleted:

Deleted: . Same as Figure 6

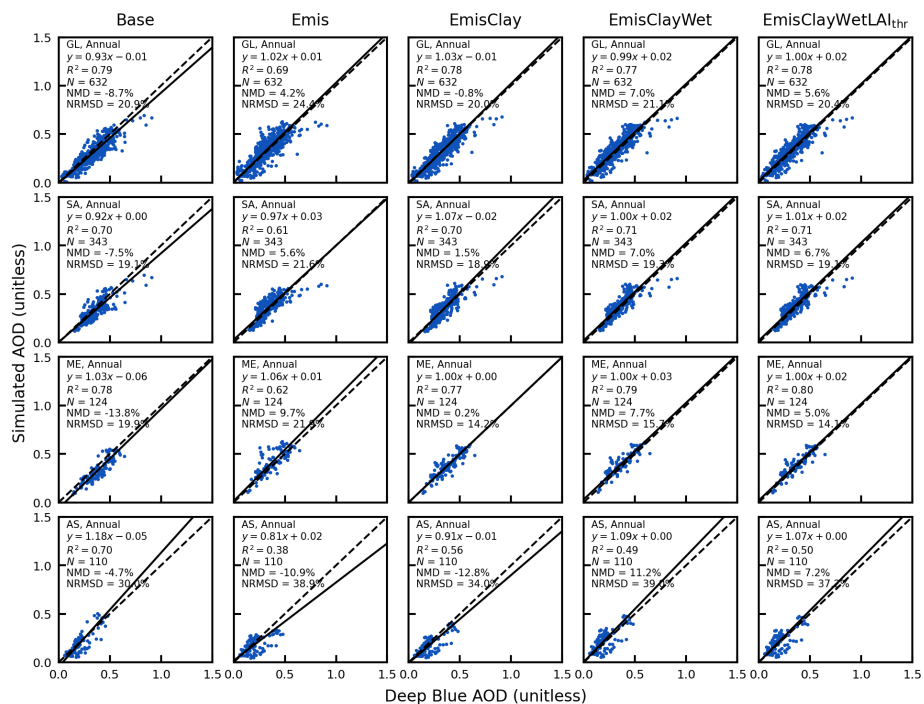


Figure A4. Same as Figure 6 but over the same dust source regions for the EmisClayWetLA1thr scheme for all dust emission scheme comparisons versus Deep Blue AOD.

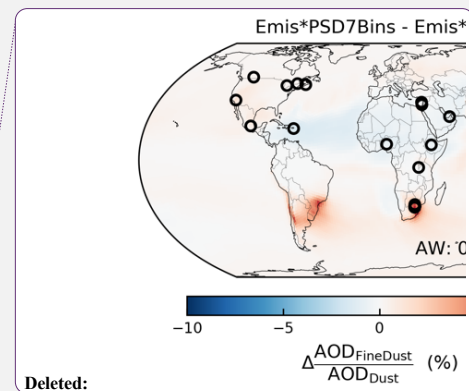
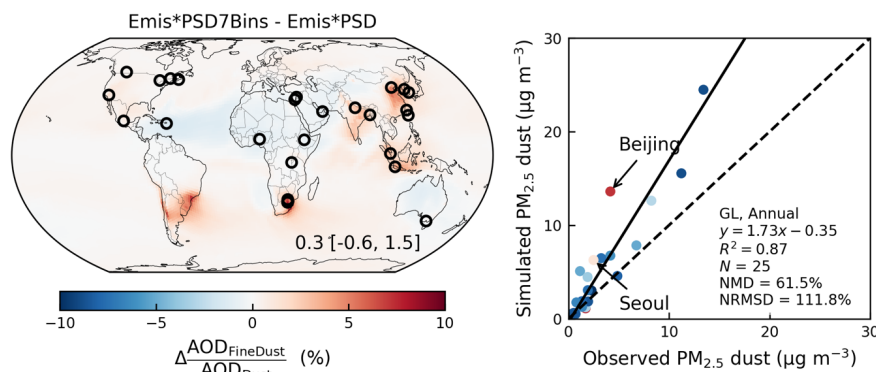
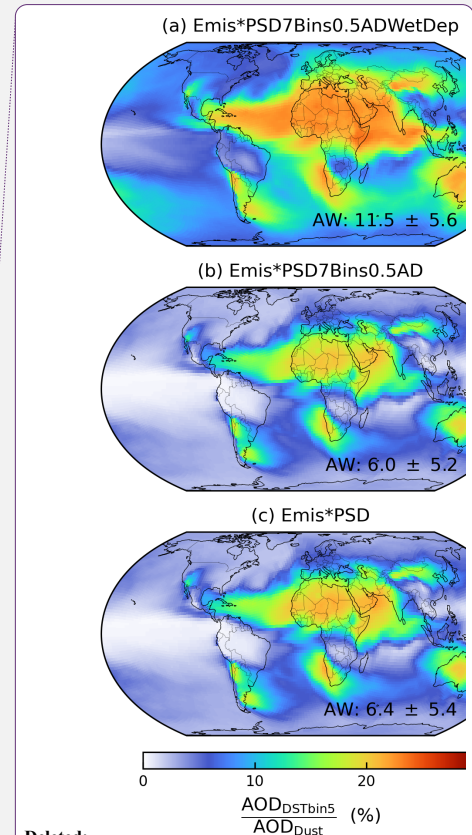
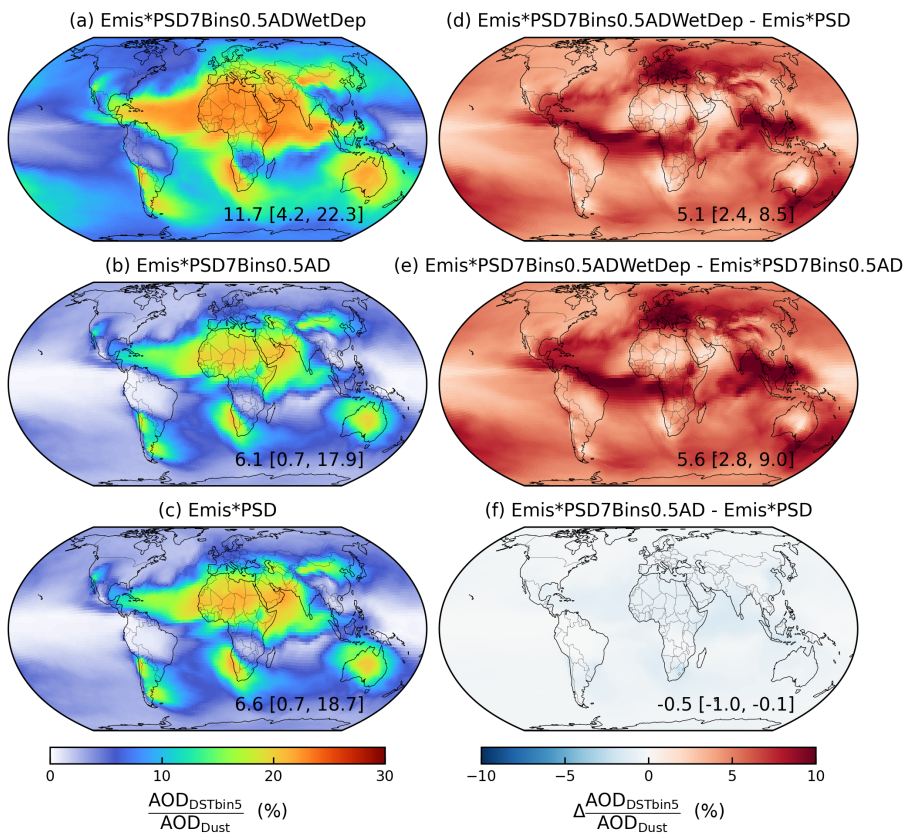


Figure A5. Differences of the fractional contributions of fine dust with geometric diameter less than $2 \mu m$ to total dust column abundance ($AOD_{FineDust} / AOD_{Dust}$) between the Emis*PSD7Bins and Emis*PSD simulations (left); Comparison between simulated $PM_{2.5}$ dust against SPARTAN measurements from the Emis*PSD7Bins simulation with color coded by the differences of $AOD_{FineDust} / AOD_{Dust}$ between the Emis*PSD7Bins and Emis*PSD simulations over SPARTAN sites. Open circles in the map indicate SPARTAN sites. Inset values at the bottom right of the map are arithmetical mean with 5th and 95th percentiles in the square brackets. Regression statistics including the reduced-major-axis linear regression equation, coefficient of variation (R^2), total number of points (N), normalized mean difference (NMD), and normalized root-mean-square difference (NRMSD) are listed at the bottom right of the scatter plot.

Deleted: area-weighted (AW)

Deleted: standard deviation

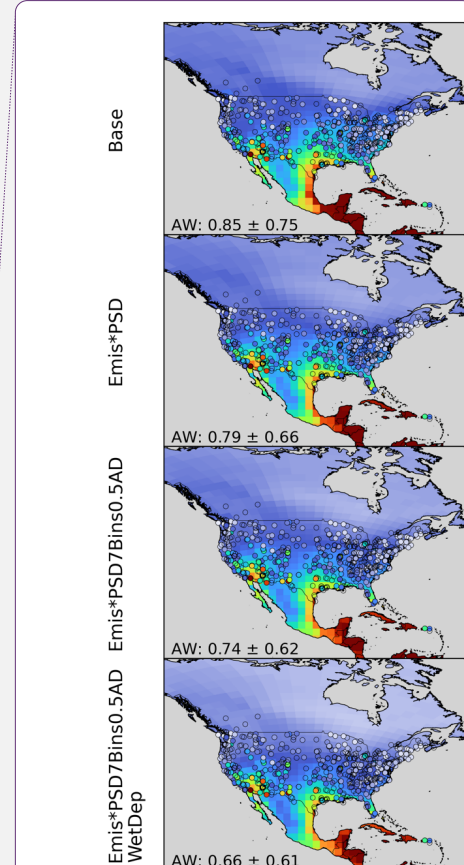
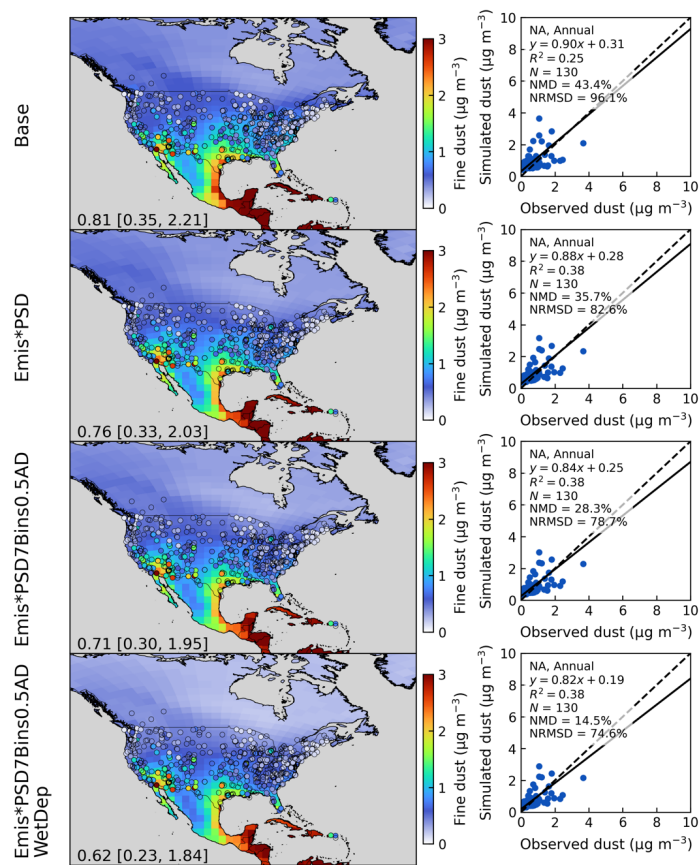


Deleted:

Deleted: area-weighted (AW)

Deleted: standard deviation

Figure A6. Fractional contributions of DSTbin5 to total dust column abundance ($AOD_{DSTbin5}/AOD_{Dust}$) from the a) Emis*PSD7Bins0.5ADWetDep, b) Emis*PSD7Bins0.5AD, c) Emis*PSD and their absolute differences. Inset values at the bottom right are arithmetical mean with 5th and 95th percentiles in the square brackets.

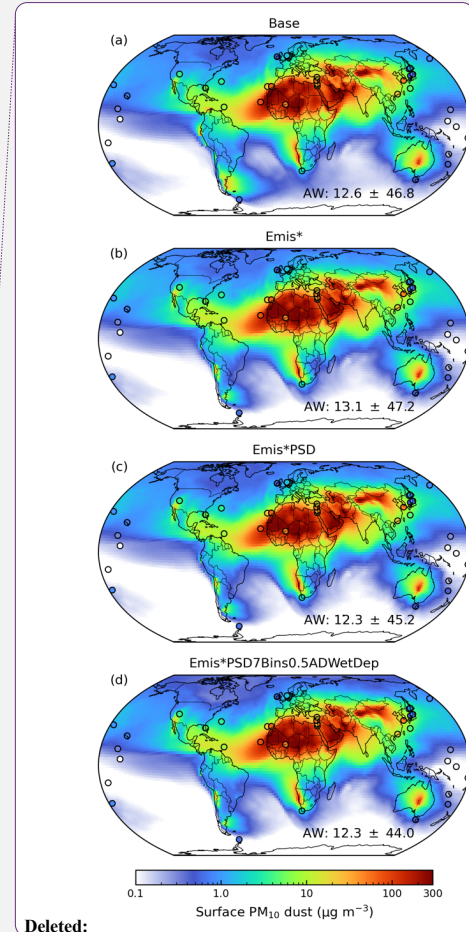
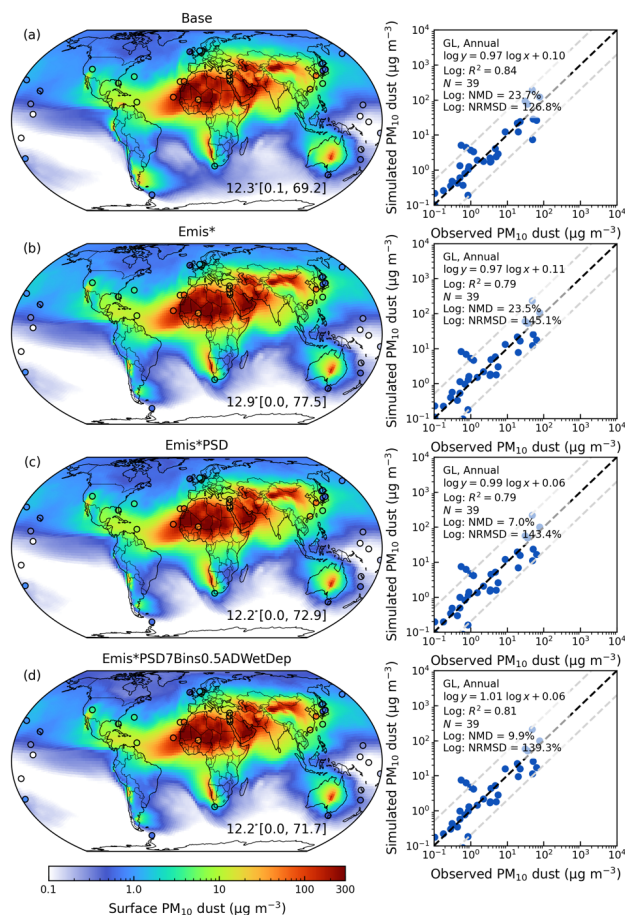


Deleted:

Deleted: area-weighted (AW)

Deleted: standard deviation

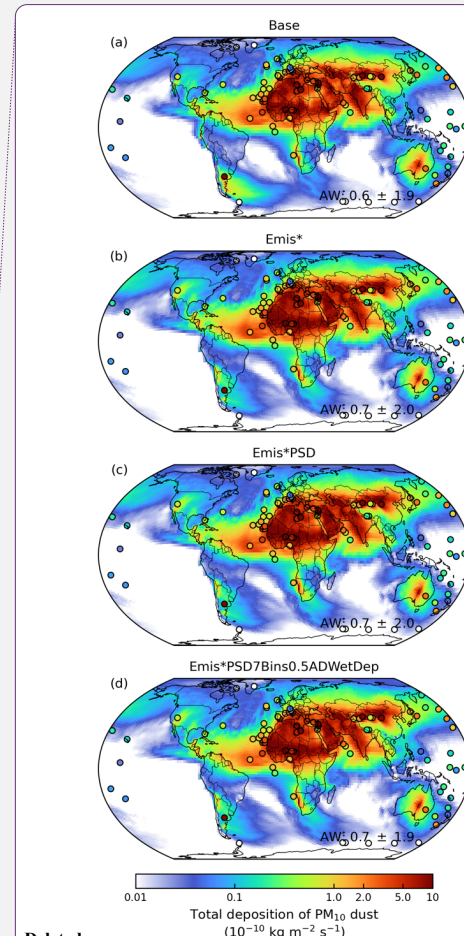
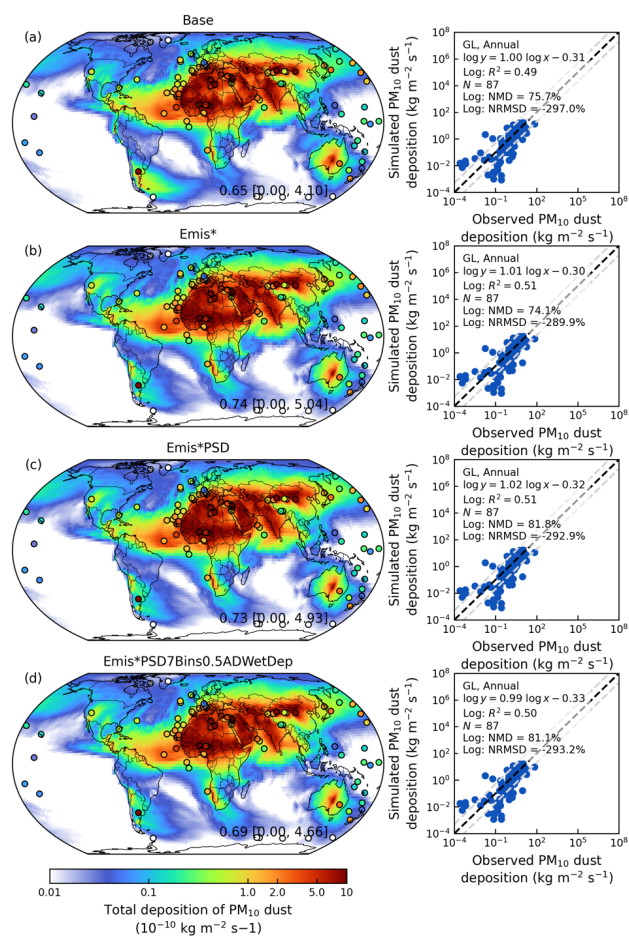
Figure A7. Comparisons of simulated annual surface $PM_{2.5}$ dust against ground-based observations in the year of 2018 over North America from the Base (top), Emis*PSD (second), Emis*PSD7Bins0.5AD (third), and Emis*PSD7Bins0.5ADWetDep (bottom) simulations. Filled circles represent ground-based observations of surface $PM_{2.5}$ dust concentrations. Inset values at the bottom left are arithmetical mean with 5th and 95th percentiles in the square brackets. Regression statistics including the reduced-major axis linear regression equation, coefficient of variation (R^2), total number of points (N), normalized mean difference (NMD), and normalized root-mean-square difference (NRMSD) are listed at the top left of right panels.



Deleted:

Deleted: area-weighted (AW)

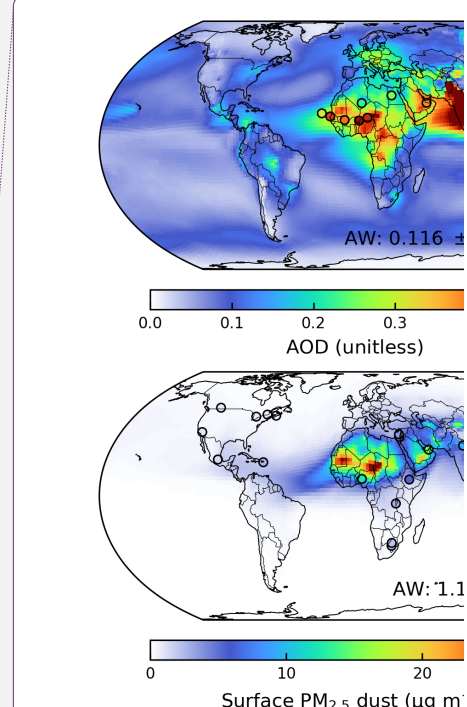
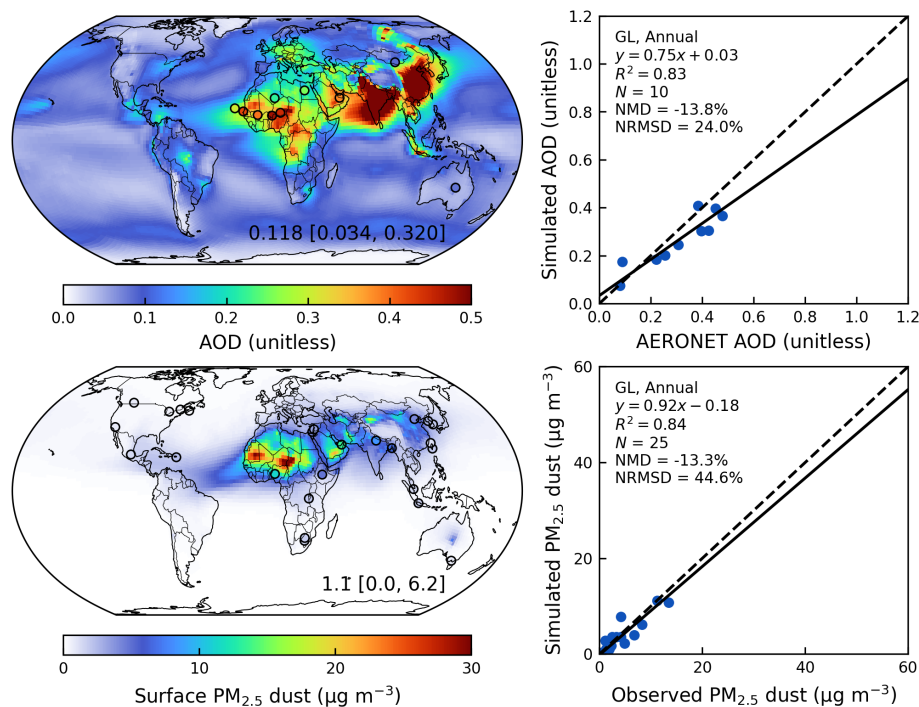
Deleted: standard deviation



Deleted:

Deleted: area-weighted (AW)

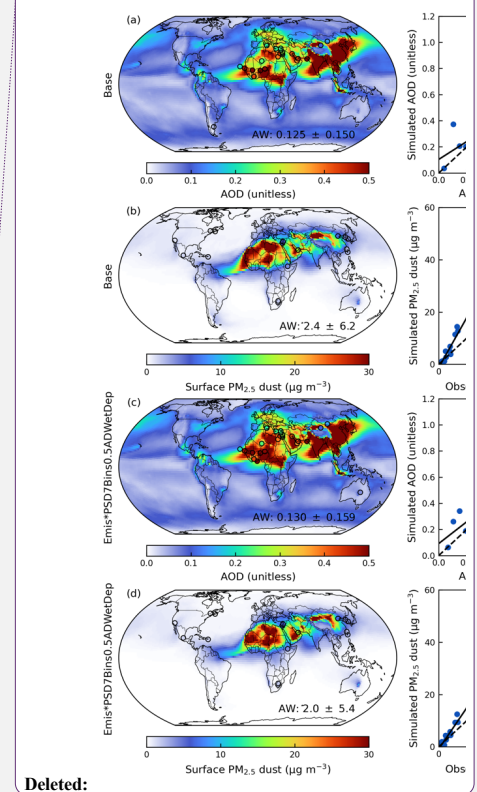
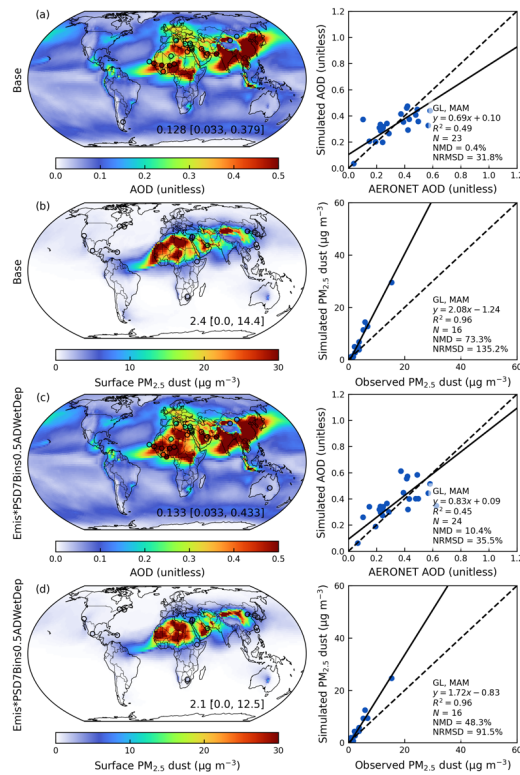
Deleted: standard deviation



Deleted:

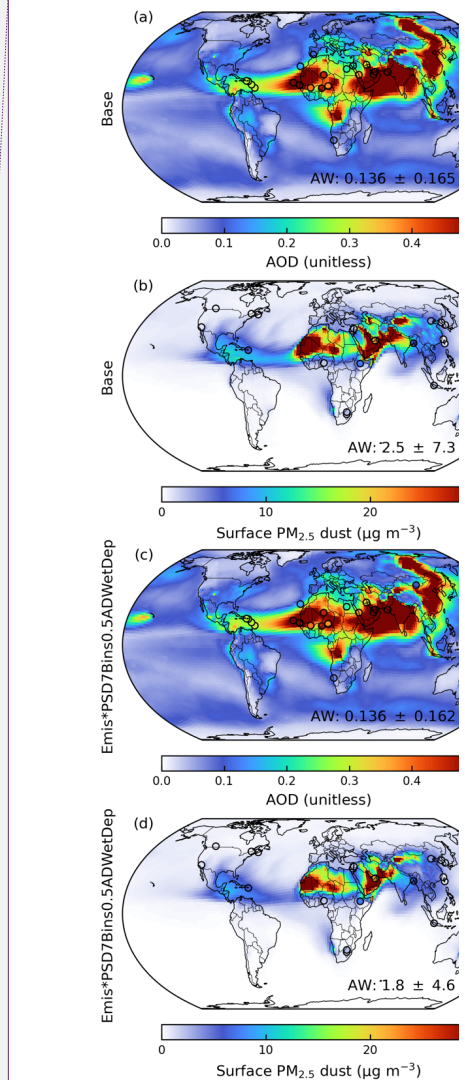
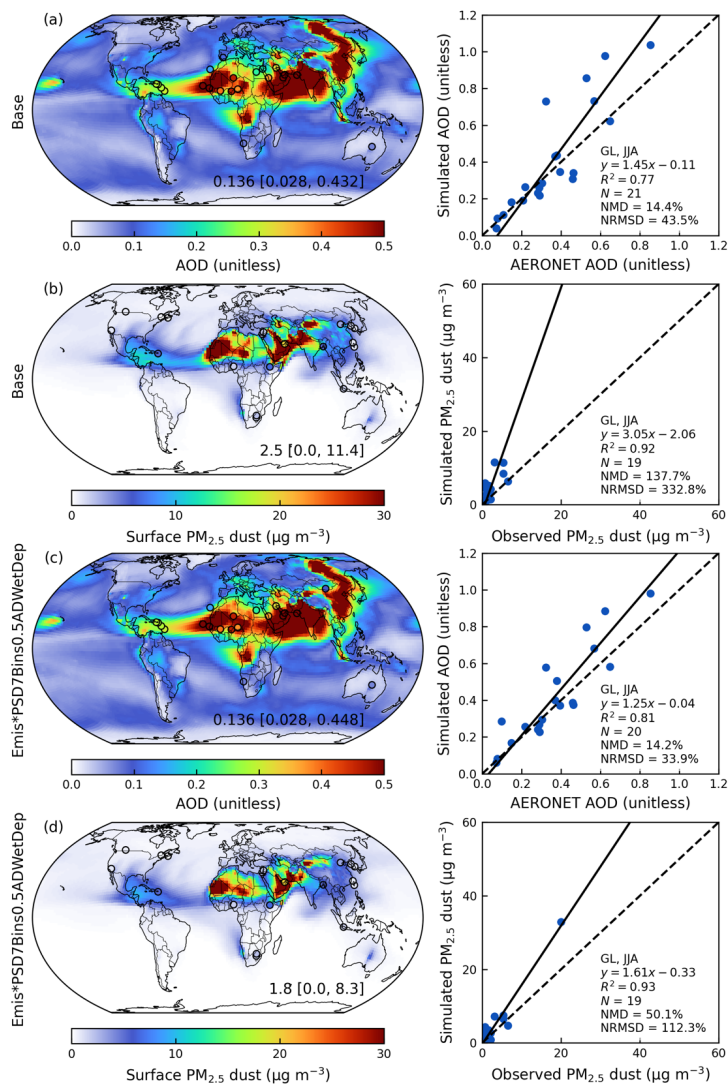
Deleted: area-weighted (AW)

Deleted: standard deviation



Deleted: area-weighted (AW)

Deleted: standard deviation



Deleted:
Figure A10.

Moved (insertion) [3]

Deleted: Figure A8

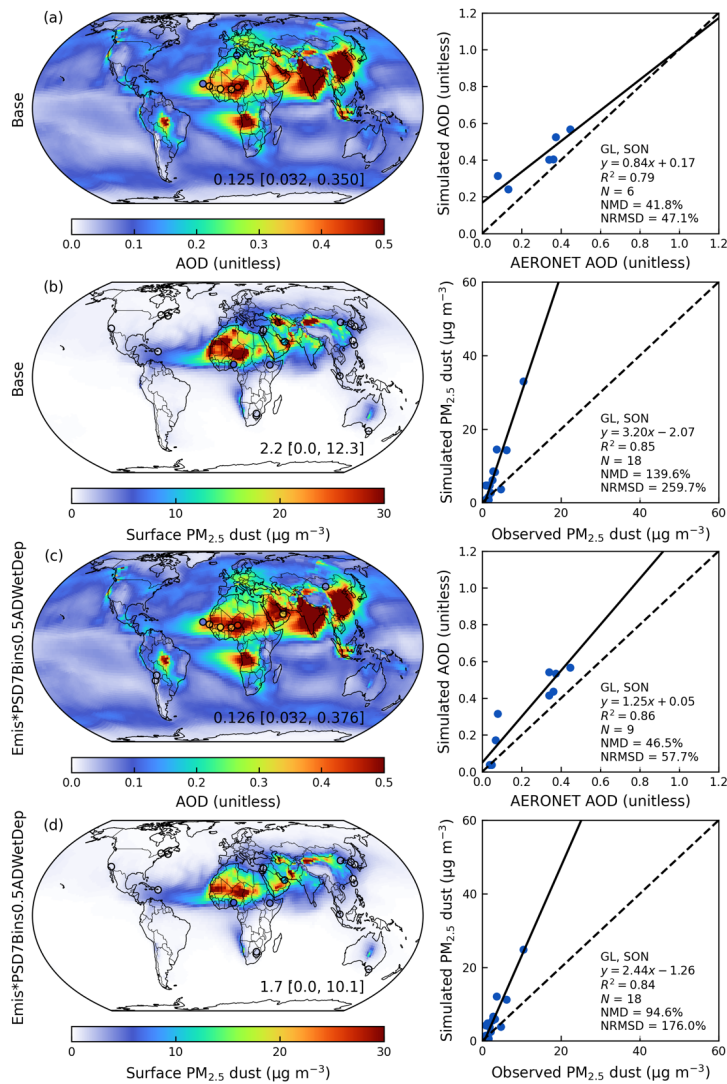
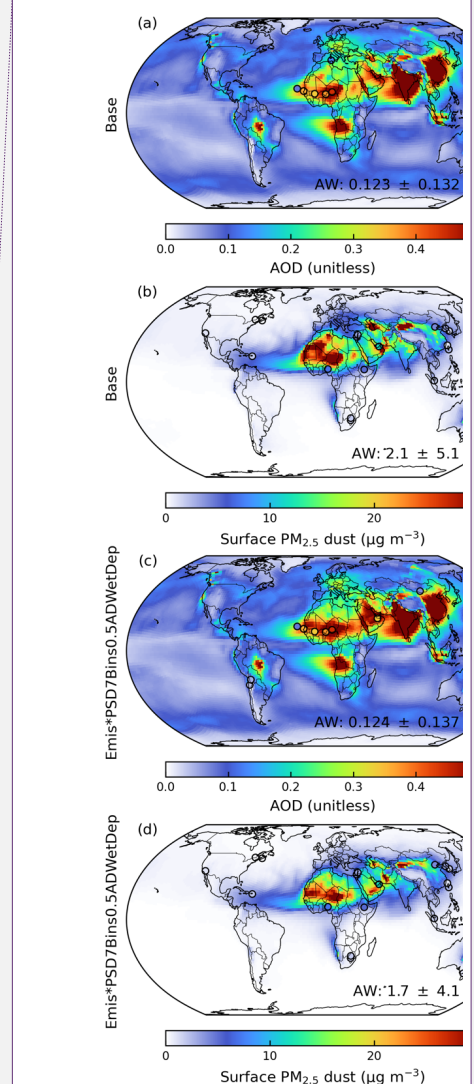


Figure A13. Same as Figure A11 but for the seasonal mean of September, October, and November (SON).



Deleted:

Deleted: Figure A8

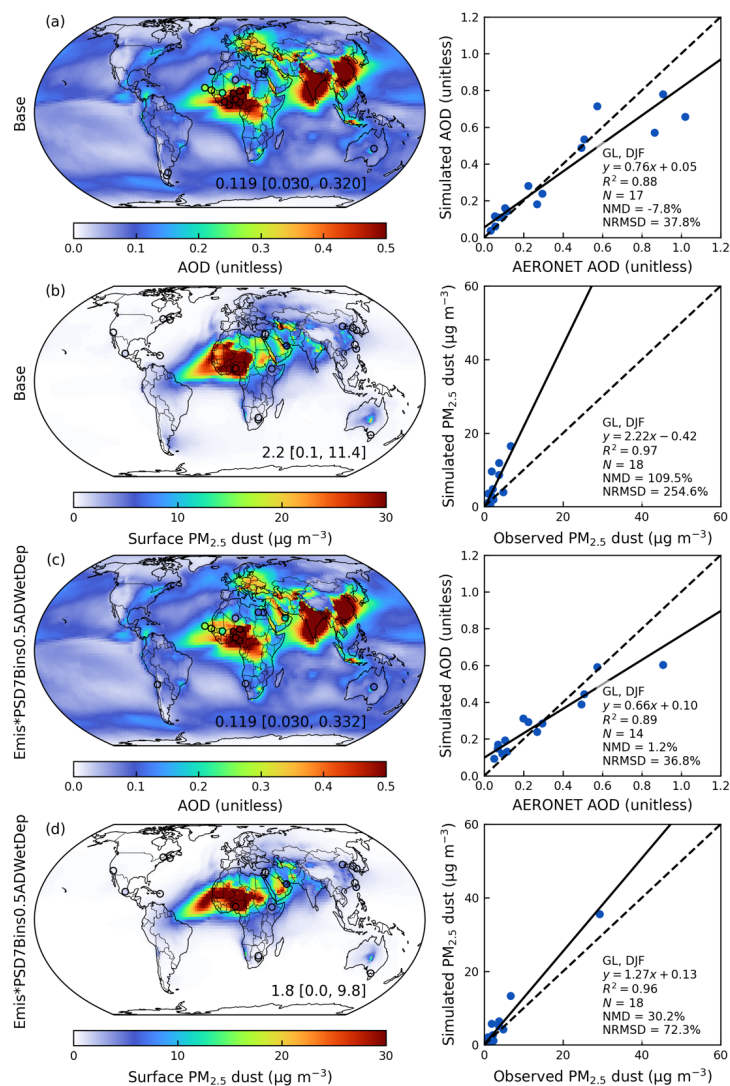


Figure A14. Same as Figure A11 but for the seasonal mean of December, January, and February (DJF).

Deleted:

Moved up [3]: Figure A12.

Deleted: Same as Figure A8

1458 **Code availability.** The standard GEOS-Chem in its high-performance configuration version 14.4.1
1459 can be downloaded at <https://doi.org/10.5281/zenodo.12584305> (The International GEOS-Chem
1460 User Community, 2024). The model source code, an example run directory, and the calculation
1461 scripts for the hourly dust emission fluxes for the revised simulation can be downloaded at
1462 <https://doi.org/10.5281/zenodo.14510793> (Zhang, 2024).

1463 **Data availability.** The surface PM_{2.5} dust measurements with the attenuation correction from
1464 SPARTAN used in this study ~~are publicly available at <https://www.spartan-network.org/data>~~ (last
1465 access: 18 March 2025). The PM₁₀ dust and total deposition of dust are available at
1466 <https://doi.org/10.5281/zenodo.6989502> (Li et al., 2022a). The processed meteorological fields
1467 from GEOS-FP are available at
1468 http://geoschemdata.wustl.edu/ExtData/GEOS_0.25x0.3125/GEOS_FP/ (last access: 4 February
1469 2025) with the soil porosity downloaded from the constant land-surface parameter of MERRA2
1470 M2C0NXLND collection (<https://disc.gsfc.nasa.gov/datasets?project=MERRA-2>, last access: 4
1471 February 2025). The land cover dataset can be downloaded at
1472 <https://lpdaac.usgs.gov/products/mcd12c1v061/> (last access: 4 February 2025). The monthly
1473 mean leaf area index at 0.5 degree can be downloaded at
1474 <http://globalchange.bnu.edu.cn/research/laiv6> (last access: 4 February 2025). The satellite-
1475 derived aeolian roughness data are available upon contacting Catherine Prigent. The GSDE soil
1476 dataset can be downloaded at <http://globalchange.bnu.edu.cn/research/soilw> (last access: 4
1477 February 2025).

1478 **Author contribution.** The manuscript was written by DZ and RVM with contributions from all
1479 authors. DZ and RVM designed the study with developments of the methodology. DZ conducted
1480 simulations and analyzed the results. XL developed the methodology for the mineral dust
1481 concentration construction in SPARTAN. AvD compiled the Deep Blue AOD dataset and ground-
1482 based observation datasets of surface PM_{2.5} dust over NA and AERONET AOD for evaluation. XL,
1483 CRO and EW contributed to SPARTAN measurements. YL contributed to the dry deposition
1484 analysis. JM offered valuable discussion for the emission scheme refinements. DML and JFK
1485 contributed to the development of a new dust emission scheme. LL constructed the observational
1486 data for PM₁₀ dust and deposition flux. HZ contributed to the generation of SPARTAN dust data. JRT
1487 and YY contributed to the discussion of the evaluation of simulated dust. MB and YR contributed to
1488 the establishment and maintenance of SPARTAN monitoring sites. All authors contributed to

Deleted: will be public

Deleted: in future release

Deleted: 4 February

1492 revising the manuscript.

1493 **Competing interests.** The authors declare no competing financial interest.

Formatted: Font: +Body (Aptos)

1494 **Acknowledgements.** This work was supported by the National Science Foundation grants
1495 2244984 and 2151093, and the National Aeronautics and Space Administration grant
1496 80NSSC22K0200. The GEOS-FP data used in this study have been provided by the Global Modeling
1497 and Assimilation Office (GMAO) at the NASA Goddard Space Flight Center. We thank the AERONET,
1498 CALIOP, MODIS, and VIIRS teams for the creation and public release of their data products.

Formatted: Font: +Body (Aptos)

1499 References

1500 [Amato, F., Schaap, M., Denier van der Gon, H. A. C., Pandolfi, M., Alastuey, A., Keuken, M., and](#)
1501 [Querol, X.: Short-term variability of mineral dust, metals and carbon emission from road dust](#)
1502 [resuspension, *Atmospheric Environment*, 74, 134–140,](#)
1503 <https://doi.org/10.1016/j.atmosenv.2013.03.037>, 2013.
1504 Bagheri, G. and Bonadonna, C.: On the drag of freely falling non-spherical particles, *Powder*
1505 *Technology*, 301, 526–544, <https://doi.org/10.1016/j.powtec.2016.06.015>, 2016.
1506 Bayon, G., Garzanti, E., Dinis, P., Beaufort, D., Barrat, J.-A., Germain, Y., Trinquier, A., Barbarano,
1507 M., Overare, B., Adeaga, O., and Braquet, N.: Contribution of Saharan dust to chemical weathering
1508 fluxes and associated phosphate release in West Africa, *Earth and Planetary Science Letters*, 641,
1509 118845, <https://doi.org/10.1016/j.epsl.2024.118845>, 2024.
1510 Bey, I., Jacob, D. J., Yantosca, R. M., Logan, J. A., Field, B. D., Fiore, A. M., Li, Q., Liu, H. Y., Mickley,
1511 L. J., and Schultz, M. G.: Global modeling of tropospheric chemistry with assimilated meteorology:
1512 Model description and evaluation, *Journal of Geophysical Research: Atmospheres*, 106, 23073–
1513 23095, <https://doi.org/10.1029/2001JD000807>, 2001.
1514 Bouwman, A. F., Lee, D. S., Asman, W. A. H., Dentener, F. J., Van Der Hoek, K. W., and Olivier, J. G.
1515 J.: A global high-resolution emission inventory for ammonia, *Global Biogeochemical Cycles*, 11,
1516 561–587, <https://doi.org/10.1029/97GB02266>, 1997.
1517 Breider, T. J., Mickley, L. J., Jacob, D. J., Ge, C., Wang, J., Payer Sulprizio, M., Croft, B., Ridley, D. A.,
1518 McConnell, J. R., Sharma, S., Husain, L., Dutkiewicz, V. A., Eleftheriadis, K., Skov, H., and Hopke, P.
1519 K.: Multidecadal trends in aerosol radiative forcing over the Arctic: Contribution of changes in

1520 anthropogenic aerosol to Arctic warming since 1980, *Journal of Geophysical Research:*
1521 *Atmospheres*, 122, 3573–3594, <https://doi.org/10.1002/2016JD025321>, 2017.

1522 [Cakmur, R. V., Miller, R. L., Perlwitz, J., Geogdzhayev, I. V., Ginoux, P., Koch, D., Kohfeld, K. E.,](#)
1523 [Tegen, I., and Zender, C. S.: Constraining the magnitude of the global dust cycle by minimizing the](#)
1524 [difference between a model and observations, *Journal of Geophysical Research: Atmospheres*,](#)
1525 [111, <https://doi.org/10.1029/2005JD005791>, 2006.](#)

1526 Cao, C., De Luccia, F. J., Xiong, X., Wolfe, R., and Weng, F.: Early On-Orbit Performance of the
1527 Visible Infrared Imaging Radiometer Suite Onboard the Suomi National Polar-Orbiting Partnership
1528 (S-NPP) Satellite, *IEEE Transactions on Geoscience and Remote Sensing*, 52, 1142–1156,
1529 <https://doi.org/10.1109/TGRS.2013.2247768>, 2014.

1530 Comola, F., Kok, J. F., Chamecki, M., and Martin, R. L.: The Intermittency of Wind-Driven Sand
1531 Transport, *Geophysical Research Letters*, 46, 13430–13440,
1532 <https://doi.org/10.1029/2019GL085739>, 2019.

1533 Croft, B., Wentworth, G. R., Martin, R. V., Leitch, W. R., Murphy, J. G., Murphy, B. N., Kodros, J. K.,
1534 Abbatt, J. P. D., and Pierce, J. R.: Contribution of Arctic seabird-colony ammonia to atmospheric
1535 particles and cloud-albedo radiative effect, *Nature Communications*, 7, 13444,
1536 <https://doi.org/10.1038/ncomms13444>, 2016.

1537 Darmenova, K., Sokolik, I. N., Shao, Y., Marticorena, B., and Bergametti, G.: Development of a
1538 physically based dust emission module within the Weather Research and Forecasting (WRF)
1539 model: Assessment of dust emission parameterizations and input parameters for source regions in
1540 Central and East Asia, *Journal of Geophysical Research: Atmospheres*, 114, D14201,
1541 <https://doi.org/10.1029/2008JD011236>, 2009.

1542 Eastham, S. D., Long, M. S., Keller, C. A., Lundgren, E., Yantosca, R. M., Zhuang, J. W., Li, C., Lee, C.
1543 J., Yannetti, M., Auer, B. M., Clune, T. L., Kouatchou, J., Putman, W. M., Thompson, M. A., Trayanov,
1544 A. L., Molod, A. M., Martin, R. V., and Jacob, D. J.: GEOS-Chem High Performance (GCHP v11-02c):
1545 a next-generation implementation of the GEOS-Chem chemical transport model for massively
1546 parallel applications, *Geoscientific Model Development*, 11, 2941–2953,
1547 <https://doi.org/10.5194/gmd-11-2941-2018>, 2018.

1548 Emerson, E. W., Hodshire, A. L., DeBolt, H. M., Bilsback, K. R., Pierce, J. R., McMeeking, G. R., and

1549 Farmer, D. K.: Revisiting particle dry deposition and its role in radiative effect estimates,
 1550 Proceedings of the National Academy of Sciences, 117, 26076–26082,
 1551 <https://doi.org/10.1073/pnas.2014761117>, 2020.

1552 Fairlie, T. D., Jacob, D. J., and Park, R. J.: The impact of transpacific transport of mineral dust in the
 1553 United States, *Atmospheric Environment*, 41, 1251–1266,
 1554 <https://doi.org/10.1016/j.atmosenv.2006.09.048>, 2007.

1555 Fécan, F., Marticorena, B., and Bergametti, G.: Parametrization of the increase of the aeolian
 1556 erosion threshold wind friction velocity due to soil moisture for arid and semi-arid areas, *Annales*
 1557 *Geophysicae*, 17, 149–157, <https://doi.org/10.1007/s00585-999-0149-7>, 1999.

1558 Feng, L., Smith, S. J., Braun, C., Crippa, M., Gidden, M. J., Hoesly, R., Klimont, Z., van Marle, M., van
 1559 den Berg, M., and van der Werf, G. R.: The generation of gridded emissions data for CMIP6,
 1560 *Geoscientific Model Development*, 13, 461–482, <https://doi.org/10.5194/gmd-13-461-2020>, 2020.

1561 Fisher, J. A., Jacob, D. J., Wang, Q., Bahreini, R., Carouge, C. C., Cubison, M. J., Dibb, J. E., Diehl, T.,
 1562 Jimenez, J. L., Lebensperger, E. M., Lu, Z., Meinders, M. B. J., Pye, H. O. T., Quinn, P. K., Sharma, S.,
 1563 Streets, D. G., Donkelaar, A. van, and Yantosca, R. M.: Sources, distribution, and acidity of sulfate–
 1564 ammonium aerosol in the Arctic in winter–spring, *Atmospheric Environment*, 45, 7301–7318,
 1565 <https://doi.org/10.1016/j.atmosenv.2011.08.030>, 2011.

1566 Giglio, L., Randerson, J. T., and van der Werf, G. R.: Analysis of daily, monthly, and annual burned
 1567 area using the fourth-generation global fire emissions database (GFED4), *Journal of Geophysical*
 1568 *Research: Biogeosciences*, 118, 317–328, <https://doi.org/10.1002/jgrg.20042>, 2013.

1569 Giles, D. M., Sinyuk, A., Sorokin, M. G., Schafer, J. S., Smirnov, A., Slutsker, I., Eck, T. F., Holben, B.
 1570 N., Lewis, J. R., Campbell, J. R., Welton, E. J., Korkin, S. V., and Lyapustin, A. I.: Advancements in
 1571 the Aerosol Robotic Network (AERONET) Version 3 database – automated near-real-time quality
 1572 control algorithm with improved cloud screening for Sun photometer aerosol optical depth (AOD)
 1573 measurements, *Atmospheric Measurement Techniques*, 12, 169–209,
 1574 <https://doi.org/10.5194/amt-12-169-2019>, 2019.

1575 Ginoux, P., Chin, M., Tegen, I., Prospero, J. M., Holben, B., Dubovik, O., and Lin, S.-J.: Sources and
 1576 distributions of dust aerosols simulated with the GOCART model, *Journal of Geophysical*
 1577 *Research: Atmospheres*, 106, 20255–20273, <https://doi.org/10.1029/2000JD000053>, 2001.

1578 González-Flórez, C., Klose, M., Alastuey, A., Dupont, S., Escribano, J., Etyemezian, V., Gonzalez-
1579 Romero, A., Huang, Y., Kandler, K., Nikolich, G., Panta, A., Querol, X., Reche, C., Yus-Díez, J., and
1580 Pérez García-Pando, C.: Insights into the size-resolved dust emission from field measurements in
1581 the Moroccan Sahara, *Atmospheric Chemistry and Physics*, 23, 7177–7212,
1582 <https://doi.org/10.5194/acp-23-7177-2023>, 2023.

1583 Harris, L., Zhou, L., Lin, S.-J., Chen, J.-H., Chen, X., Gao, K., Morin, M., Rees, S., Sun, Y., Tong, M.,
1584 Xiang, B., Bender, M., Benson, R., Cheng, K.-Y., Clark, S., Elbert, O. D., Hazelton, A., Huff, J. J.,
1585 Kaltenbaugh, A., Liang, Z., Marchok, T., Shin, H. H., and Stern, W.: GFDL SHiELD: A Unified System
1586 for Weather-to-Seasonal Prediction, *Journal of Advances in Modeling Earth Systems*, 12,
1587 e2020MS002223, <https://doi.org/10.1029/2020MS002223>, 2020.

1588 Hsu, N. C., Lee, J., Sayer, A. M., Kim, W., Bettenhausen, C., and Tsay, S.-C.: VIIRS Deep Blue
1589 Aerosol Products Over Land: Extending the EOS Long-Term Aerosol Data Records, *Journal of*
1590 *Geophysical Research: Atmospheres*, 124, 4026–4053, <https://doi.org/10.1029/2018JD029688>,
1591 2019.

1592 Hu, L., Keller, C. A., Long, M. S., Sherwen, T., Auer, B., Da Silva, A., Nielsen, J. E., Pawson, S.,
1593 Thompson, M. A., Trayanov, A. L., Travis, K. R., Grange, S. K., Evans, M. J., and Jacob, D. J.: Global
1594 simulation of tropospheric chemistry at 12.5 km resolution: performance and evaluation of the
1595 GEOS-Chem chemical module (v10-1) within the NASA GEOS Earth system model (GEOS-5 ESM),
1596 *Geoscientific Model Development*, 11, 4603–4620, <https://doi.org/10.5194/gmd-11-4603-2018>,
1597 2018.

1598 Huang, Y., Kok, J. F., Kandler, K., Lindqvist, H., Nousiainen, T., Sakai, T., Adebisi, A., and Jokinen,
1599 O.: Climate Models and Remote Sensing Retrievals Neglect Substantial Desert Dust Asphericity,
1600 *Geophysical Research Letters*, 47, e2019GL086592, <https://doi.org/10.1029/2019GL086592>, 2020.

1601 Huang, Y., Adebisi, A. A., Formenti, P., and Kok, J. F.: Linking the Different Diameter Types of
1602 Aspherical Desert Dust Indicates That Models Underestimate Coarse Dust Emission, *Geophysical*
1603 *Research Letters*, 48, e2020GL092054, <https://doi.org/10.1029/2020GL092054>, 2021.

1604 Huneeus, N., Schulz, M., Balkanski, Y., Griesfeller, J., Prospero, J., Kinne, S., Bauer, S., Boucher, O.,
1605 Chin, M., Dentener, F., Diehl, T., Easter, R., Fillmore, D., Ghan, S., Ginoux, P., Grini, A., Horowitz, L.,
1606 Koch, D., Krol, M. C., Landing, W., Liu, X., Mahowald, N., Miller, R., Morcrette, J.-J., Myhre, G.,
1607 Penner, J., Perlwitz, J., Stier, P., Takemura, T., and Zender, C. S.: Global dust model

1608 intercomparison in AeroCom phase I, *Atmospheric Chemistry and Physics*, 11, 7781–7816,
1609 <https://doi.org/10.5194/acp-11-7781-2011>, 2011.

1610 Iversen, J. D. and White, B. R.: Saltation threshold on Earth, Mars and Venus, *Sedimentology*, 29,
1611 111–119, <https://doi.org/10.1111/j.1365-3091.1982.tb01713.x>, 1982.

1612 Jaeglé, L., Quinn, P. K., Bates, T. S., Alexander, B., and Lin, J.-T.: Global distribution of sea salt
1613 aerosols: new constraints from in situ and remote sensing observations, *Atmospheric Chemistry
1614 and Physics*, 11, 3137–3157, <https://doi.org/10.5194/acp-11-3137-2011>, 2011.

1615 Jickells, T. D., An, Z. S., Andersen, K. K., Baker, A. R., Bergametti, G., Brooks, N., Cao, J. J., Boyd, P.
1616 W., Duce, R. A., Hunter, K. A., Kawahata, H., Kubilay, N., laRoche, J., Liss, P. S., Mahowald, N.,
1617 Prospero, J. M., Ridgwell, A. J., Tegen, I., and Torres, R.: Global Iron Connections Between Desert
1618 Dust, Ocean Biogeochemistry, and Climate, *Science*, 308, 67–71,
1619 <https://doi.org/10.1126/science.1105959>, 2005.

1620 Jones, A. C., Hill, A., Hemmings, J., Lemaître, P., Quétel, A., Ryder, C. L., and Woodward, S.: Below-
1621 cloud scavenging of aerosol by rain: a review of numerical modelling approaches and sensitivity
1622 simulations with mineral dust in the Met Office’s Unified Model, *Atmospheric Chemistry and
1623 Physics*, 22, 11381–11407, <https://doi.org/10.5194/acp-22-11381-2022>, 2022.

1624 Kenny, L. C., Gussman, R., and Meyer, M.: Development of a Sharp-Cut Cyclone for Ambient
1625 Aerosol Monitoring Applications, *Aerosol Science and Technology*, 32, 338–358,
1626 <https://doi.org/10.1080/027868200303669>, 2000.

1627 Kok, J. F.: A scaling theory for the size distribution of emitted dust aerosols suggests climate
1628 models underestimate the size of the global dust cycle, *Proceedings of the National Academy of
1629 Sciences*, 108, 1016–1021, <https://doi.org/10.1073/pnas.1014798108>, 2011.

1630 Kok, J. F., Mahowald, N. M., Fratini, G., Gillies, J. A., Ishizuka, M., Leys, J. F., Mikami, M., Park, M.-S.,
1631 Park, S.-U., Van Pelt, R. S., and Zobeck, T. M.: An improved dust emission model – Part 1: Model
1632 description and comparison against measurements, *Atmospheric Chemistry and Physics*, 14,
1633 13023–13041, <https://doi.org/10.5194/acp-14-13023-2014>, 2014.

1634 Kok, J. F., Ridley, D. A., Zhou, Q., Miller, R. L., Zhao, C., Heald, C. L., Ward, D. S., Albani, S., and
1635 Haustein, K.: Smaller desert dust cooling effect estimated from analysis of dust size and
1636 abundance, *Nature Geoscience*, 10, 274–278, <https://doi.org/10.1038/ngeo2912>, 2017.

1637 Kok, J. F., Adebisi, A. A., Albani, S., Balkanski, Y., Checa-Garcia, R., Chin, M., Colarco, P. R.,
 1638 Hamilton, D. S., Huang, Y., Ito, A., Klose, M., Li, L., Mahowald, N. M., Miller, R. L., Obiso, V., Pérez
 1639 García-Pando, C., Rocha-Lima, A., and Wan, J. S.: [Contribution of the world's main dust source](#)
 1640 [regions to the global cycle of desert dust](#), *Atmos. Chem. Phys.*, 21, 8169–8193,
 1641 <https://doi.org/10.5194/acp-21-8169-2021>, 2021a.
 1642 [Kok, J. F., Adebisi, A. A., Albani, S., Balkanski, Y., Checa-Garcia, R., Chin, M., Colarco, P. R.,](#)
 1643 [Hamilton, D. S., Huang, Y., Ito, A., Klose, M., Leung, D. M., Li, L., Mahowald, N. M., Miller, R. L.,](#)
 1644 [Obiso, V., Pérez García-Pando, C., Rocha-Lima, A., Wan, J. S., and Whicker, C. A.: Improved](#)
 1645 [representation of the global dust cycle using observational constraints on dust properties and](#)
 1646 [abundance](#), *Atmospheric Chemistry and Physics*, 21, 8127–8167, [https://doi.org/10.5194/acp-21-](https://doi.org/10.5194/acp-21-8127-2021)
 1647 [8127-2021](#), 2021b.
 1648 [Koster, R. D., Reichle, R. H., Mahanama, S. P., Perket, J., Liu, Q., and Partyka, G.: Land-focused](#)
 1649 [changes in the updated GEOS FP system \(Version 5.25\), 2020.](#)
 1650 Latimer, R. N. C. and Martin, R. V.: Interpretation of measured aerosol mass scattering efficiency
 1651 over North America using a chemical transport model, *Atmospheric Chemistry and Physics*, 19,
 1652 2635–2653, <https://doi.org/10.5194/acp-19-2635-2019>, 2019.
 1653 Leung, D. M., Kok, J. F., Li, L., Okin, G. S., Prigent, C., Klose, M., Pérez García-Pando, C., Menut, L.,
 1654 Mahowald, N. M., Lawrence, D. M., and Chamecki, M.: A new process-based and scale-aware
 1655 desert dust emission scheme for global climate models – Part I: Description and evaluation against
 1656 inverse modeling emissions, *Atmospheric Chemistry and Physics*, 23, 6487–6523,
 1657 <https://doi.org/10.5194/acp-23-6487-2023>, 2023.
 1658 Leung, D. M., Kok, J. F., Li, L., Mahowald, N. M., Lawrence, D. M., Tilmes, S., Kluzek, E., Klose, M.,
 1659 and Pérez García-Pando, C.: A new process-based and scale-aware desert dust emission scheme
 1660 for global climate models – Part II: Evaluation in the Community Earth System Model version 2
 1661 (CESM2), *Atmospheric Chemistry and Physics*, 24, 2287–2318, [https://doi.org/10.5194/acp-24-](https://doi.org/10.5194/acp-24-2287-2024)
 1662 [2287-2024](#), 2024.
 1663 Li, C., Martin, R. V., van Donkelaar, A., Boys, B. L., Hammer, M. S., Xu, J.-W., Marais, E. A., Reff, A.,
 1664 Strum, M., Ridley, D. A., Crippa, M., Brauer, M., and Zhang, Q.: [Trends in Chemical Composition of](#)
 1665 [Global and Regional Population-Weighted Fine Particulate Matter Estimated for 25 Years](#), *Environ.*
 1666 [Sci. Technol.](#), 51, 11185–11195, <https://doi.org/10.1021/acs.est.7b02530>, 2017.

Deleted: Leung, D. M.,

Deleted: ., and Whicker, C. A.: Improved representation

Deleted: dust

Deleted: using observational constraints on

Deleted: properties and abundance, Atmospheric Chemistry and Physics,...

Deleted: 8127–8167

Deleted: 8127

Deleted: 2021

1676 Li, L., Mahowald, N. M., Kok, J. F., Liu, X., Wu, M., Leung, D. M., Hamilton, D. S., Emmons, L. K.,
 1677 Huang, Y., Sexton, N., Meng, J., and Wan, J.: Data and codes for “Importance of different
 1678 parameterization changes for the updated dust cycle modelling in the Community Atmosphere
 1679 Model (version 6.1),” <https://doi.org/10.5281/zenodo.6989502>, 2022a.

1680 Li, L., Mahowald, N. M., Kok, J. F., Liu, X., Wu, M., Leung, D. M., Hamilton, D. S., Emmons, L. K.,
 1681 Huang, Y., Sexton, N., Meng, J., and Wan, J.: Importance of different parameterization changes for
 1682 the updated dust cycle modeling in the Community Atmosphere Model (version 6.1), *Geoscientific
 1683 Model Development*, 15, 8181–8219, <https://doi.org/10.5194/gmd-15-8181-2022>, 2022b.

1684 Liao, H. and Seinfeld, J. H.: Radiative forcing by mineral dust aerosols: Sensitivity to key variables,
 1685 *Journal of Geophysical Research: Atmospheres*, 103, 31637–31645,
 1686 <https://doi.org/10.1029/1998JD200036>, 1998.

1687 Lin, H., Jacob, D. J., Lundgren, E. W., Sulprizio, M. P., Keller, C. A., Fritz, T. M., Eastham, S. D.,
 1688 Emmons, L. K., Campbell, P. C., Baker, B., Saylor, R. D., and Montuoro, R.: Harmonized Emissions
 1689 Component (HEMCO) 3.0 as a versatile emissions component for atmospheric models: application
 1690 in the GEOS-Chem, NASA GEOS, WRF-GC, CESM2, NOAA GEFS-Aerosol, and NOAA UFS models,
 1691 *Geosci. Model Dev.*, 14, 5487–5506, <https://doi.org/10.5194/gmd-14-5487-2021>, 2021.

1692 Liu, H., Jacob, D. J., Bey, I., and Yantosca, R. M.: Constraints from ²¹⁰Pb and ⁷Be on wet deposition
 1693 and transport in a global three-dimensional chemical tracer model driven by assimilated
 1694 meteorological fields, *Journal of Geophysical Research: Atmospheres*, 106, 12109–12128,
 1695 <https://doi.org/10.1029/2000JD900839>, 2001.

1696 Liu, X., Turner, J. R., Hand, J. L., Schichtel, B. A., and Martin, R. V.: A Global-Scale Mineral Dust
 1697 Equation, *Journal of Geophysical Research: Atmospheres*, 127, e2022JD036937,
 1698 <https://doi.org/10.1029/2022JD036937>, 2022.

1699 Liu, X., Turner, J. R., Oxford, C. R., McNeill, J., Walsh, B., Le Roy, E., Weagle, C. L., Stone, E., Zhu,
 1700 H., Liu, W., Wei, Z., Hyslop, N. P., Giacomo, J., Dillner, A. M., Salam, A., Hossen, A., Islam, Z.,
 1701 Abboud, I., Akoshile, C., Amador-Muñoz, O., Anh, N. X., Asfaw, A., Balasubramanian, R., Chang, R.
 1702 Y.-W., Coburn, C., Dey, S., Diner, D. J., Dong, J., Farrah, T., Gahungu, P., Garland, R. M., Grutter de
 1703 la Mora, M., Hasheminassab, S., John, J., Kim, J., Kim, J. S., Langerman, K., Lee, P.-C., Lestari, P.,
 1704 Liu, Y., Mamo, T., Martins, M., Mayol-Bracero, O. L., Naidoo, M., Park, S. S., Schechner, Y.,
 1705 Schofield, R., Tripathi, S. N., Windwer, E., Wu, M.-T., Zhang, Q., Brauer, M., Rudich, Y., and Martin,

1706 R. V.: Elemental Characterization of Ambient Particulate Matter for a Globally Distributed
 1707 Monitoring Network: Methodology and Implications, *ACS EST Air*, 1, 283–293,
 1708 <https://doi.org/10.1021/acsestair.3c00069>, 2024.

1709 Mahowald, N., Kohfeld, K., Hansson, M., Balkanski, Y., Harrison, S. P., Prentice, I. C., Schulz, M.,
 1710 and Rodhe, H.: Dust sources and deposition during the last glacial maximum and current climate:
 1711 A comparison of model results with paleodata from ice cores and marine sediments, *Journal of*
 1712 *Geophysical Research: Atmospheres*, 104, 15895–15916, <https://doi.org/10.1029/1999JD900084>,
 1713 1999.

1714 Mahowald, N., Albani, S., Kok, J. F., Engelstaeder, S., Scanza, R., Ward, D. S., and Flanner, M. G.:
 1715 The size distribution of desert dust aerosols and its impact on the Earth system, *Aeolian Research*,
 1716 15, 53–71, <https://doi.org/10.1016/j.aeolia.2013.09.002>, 2014.

1717 Marticorena, B. and Bergametti, G.: Modeling the atmospheric dust cycle: 1. Design of a soil-
 1718 derived dust emission scheme, *Journal of Geophysical Research: Atmospheres*, 100, 16415–
 1719 16430, <https://doi.org/10.1029/95JD00690>, 1995.

1720 Martin, R. L. and Kok, J. F.: Distinct Thresholds for the Initiation and Cessation of Aeolian Saltation
 1721 From Field Measurements, *Journal of Geophysical Research: Earth Surface*, 123, 1546–1565,
 1722 <https://doi.org/10.1029/2017JF004416>, 2018.

1723 Martin, R. V., Eastham, S. D., Bindle, L., Lundgren, E. W., Clune, T. L., Keller, C. A., Downs, W.,
 1724 Zhang, D., Lucchesi, R. A., Sulprizio, M. P., Yantosca, R. M., Li, Y., Estrada, L., Putman, W. M., Auer,
 1725 B. M., Trayanov, A. L., Pawson, S., and Jacob, D. J.: Improved advection, resolution, performance,
 1726 and community access in the new generation (version 13) of the high-performance GEOS-Chem
 1727 global atmospheric chemistry model (GCHP), *Geoscientific Model Development*, 15, 8731–8748,
 1728 <https://doi.org/10.5194/gmd-15-8731-2022>, 2022.

1729 Meng, J., Martin, R. V., Ginoux, P., Hammer, M., Sulprizio, M. P., Ridley, D. A., and van Donkelaar,
 1730 A.: Grid-independent high-resolution dust emissions (v1.0) for chemical transport models:
 1731 application to GEOS-Chem (12.5.0), *Geoscientific Model Development*, 14, 4249–4260,
 1732 <https://doi.org/10.5194/gmd-14-4249-2021>, 2021.

1733 Meng, J., Huang, Y., Leung, D. M., Li, L., Adebisi, A. A., Ryder, C. L., Mahowald, N. M., and Kok, J. F.:
 1734 Improved Parameterization for the Size Distribution of Emitted Dust Aerosols Reduces Model

1735 Underestimation of Super Coarse Dust, *Geophysical Research Letters*, 49, e2021GL097287,
1736 <https://doi.org/10.1029/2021GL097287>, 2022.

1737 Miller, S. J., Makar, P. A., and Lee, C. J.: HETerogeneous vectorized or Parallel (HETPv1.0): an
1738 updated inorganic heterogeneous chemistry solver for the metastable-state $\text{NH}_4^+ - \text{Na}^+ - \text{Ca}^{2+} - \text{K}^+ -$
1739 $\text{Mg}^{2+} - \text{SO}_4^{2-} - \text{NO}_3^- - \text{Cl}^- - \text{H}_2\text{O}$ system based on ISORROPIA II, *Geoscientific Model Development*, 17,
1740 2197–2219, <https://doi.org/10.5194/gmd-17-2197-2024>, 2024.

1741 Murray, L. T., Jacob, D. J., Logan, J. A., Hudman, R. C., and Koshak, W. J.: Optimized regional and
1742 interannual variability of lightning in a global chemical transport model constrained by LIS/OTD
1743 satellite data, *Journal of Geophysical Research: Atmospheres*, 117, D20307,
1744 <https://doi.org/10.1029/2012JD017934>, 2012.

1745 Mytilinaios, M., Basart, S., Ciamprone, S., Cuesta, J., Dema, C., Di Tomaso, E., Formenti, P.,
1746 Gkikas, A., Jorba, O., Kahn, R., Pérez García-Pando, C., Trippetta, S., and Mona, L.: Comparison of
1747 dust optical depth from multi-sensor products and MONARCH (Multiscale Online Non-hydrostatic
1748 AtmospheRe CHEmistry) dust reanalysis over North Africa, the Middle East, and Europe,
1749 *Atmospheric Chemistry and Physics*, 23, 5487–5516, <https://doi.org/10.5194/acp-23-5487-2023>,
1750 2023.

1751 Okin, G. S.: A new model of wind erosion in the presence of vegetation, *Journal of Geophysical*
1752 *Research: Earth Surface*, 113, <https://doi.org/10.1029/2007JF000758>, 2008.

1753 Pai, S. J., Heald, C. L., Pierce, J. R., Farina, S. C., Marais, E. A., Jimenez, J. L., Campuzano-Jost, P.,
1754 Nault, B. A., Middlebrook, A. M., Coe, H., Shilling, J. E., Bahreini, R., Dingle, J. H., and Vu, K.: An
1755 evaluation of global organic aerosol schemes using airborne observations, *Atmospheric Chemistry*
1756 *and Physics*, 20, 2637–2665, <https://doi.org/10.5194/acp-20-2637-2020>, 2020.

1757 Panofsky, H. A., Tennekes, H., Lenschow, D. H., and Wyngaard, J. C.: The characteristics of
1758 turbulent velocity components in the surface layer under convective conditions, *Boundary-Layer*
1759 *Meteorology*, 11, 355–361, <https://doi.org/10.1007/BF02186086>, 1977.

1760 Park, R. J., Jacob, D. J., Field, B. D., Yantosca, R. M., and Chin, M.: Natural and transboundary
1761 pollution influences on sulfate-nitrate-ammonium aerosols in the United States: Implications for
1762 policy, *Journal of Geophysical Research: Atmospheres*, 109, D15204,
1763 <https://doi.org/10.1029/2003jd004473>, 2004.

Deleted: NH_4^{+} —

Deleted: $\text{SO}_4^{2-} - \text{NO}_3^-$ —

Deleted: $^- \text{H}_2\text{O}$

1767 Peters, T. M., Kenny, L. C., Gussman, R. A., and Vanderpool, R. W.: Evaluation of PM2.5 Size
 1768 Selectors Used in Speciation Samplers, *Aerosol Science and Technology*, 34, 422–429,
 1769 <https://doi.org/10.1080/02786820119266>, 2001.

1770 Petroff, A. and Zhang, L.: Development and validation of a size-resolved particle dry deposition
 1771 scheme for application in aerosol transport models, *Geoscientific Model Development*, 3, 753–
 1772 769, <https://doi.org/10.5194/gmd-3-753-2010>, 2010.

1773 Philip, S., Martin, R. V., Snider, G., Weagle, C. L., Donkelaar, A. van, Brauer, M., Henze, D. K.,
 1774 Klimont, Z., Venkataraman, C., Guttikunda, S. K., and Zhang, Q.: Anthropogenic fugitive,
 1775 combustion and industrial dust is a significant, underrepresented fine particulate matter source in
 1776 global atmospheric models, *Environmental Research Letters*, 12, 044018,
 1777 <https://doi.org/10.1088/1748-9326/aa65a4>, 2017.

1778 Pierre, C., Bergametti, G., Marticorena, B., Kergoat, L., Mougin, E., and Hiernaux, P.: Comparing
 1779 drag partition schemes over a herbaceous Sahelian rangeland, *Journal of Geophysical Research:*
 1780 *Earth Surface*, 119, 2291–2313, <https://doi.org/10.1002/2014JF003177>, 2014a.

1781 Pierre, C., Bergametti, G., Marticorena, B., AbdourhamaneTouré, A., Rajot, J.-L., and Kergoat, L.:
 1782 Modeling wind erosion flux and its seasonality from a cultivated sahelian surface: A case study in
 1783 Niger, *CATENA*, 122, 61–71, <https://doi.org/10.1016/j.catena.2014.06.006>, 2014b.

1784 Poggio, L., de Sousa, L. M., Batjes, N. H., Heuvelink, G. B. M., Kempen, B., Ribeiro, E., and Rossiter,
 1785 D.: SoilGrids 2.0: producing soil information for the globe with quantified spatial uncertainty, *SOIL*,
 1786 7, 217–240, <https://doi.org/10.5194/soil-7-217-2021>, 2021.

1787 Prigent, C., Tegen, I., Aires, F., Marticorena, B., and Zribi, M.: Estimation of the aerodynamic
 1788 roughness length in arid and semi-arid regions over the globe with the ERS scatterometer, *Journal*
 1789 *of Geophysical Research: Atmospheres*, 110, <https://doi.org/10.1029/2004JD005370>, 2005.

1790 Prospero, J. M.: Long-range transport of mineral dust in the global atmosphere: Impact of African
 1791 dust on the environment of the southeastern United States, *Proceedings of the National Academy*
 1792 *of Sciences*, 96, 3396–3403, <https://doi.org/10.1073/pnas.96.7.3396>, 1999.

1793 [Reid, J. S., Jonsson, H. H., Maring, H. B., Smirnov, A., Savoie, D. L., Cliff, S. S., Reid, E. A.,](#)
 1794 [Livingston, J. M., Meier, M. M., Dubovik, O., and Tsay, S.-C.: Comparison of size and morphological](#)
 1795 [measurements of coarse mode dust particles from Africa, *Journal of Geophysical Research:*](#)

1796 [Atmospheres, 108, https://doi.org/10.1029/2002JD002485, 2003.](https://doi.org/10.1029/2002JD002485)

1797 Ridley, D. A., Heald, C. L., and Ford, B.: North African dust export and deposition: A satellite and

1798 model perspective, *Journal of Geophysical Research: Atmospheres*, 117, D02202,

1799 <https://doi.org/10.1029/2011JD016794>, 2012.

1800 Ridley, D. A., Heald, C. L., Kok, J. F., and Zhao, C.: An observationally constrained estimate of

1801 global dust aerosol optical depth, *Atmospheric Chemistry and Physics*, 16, 15097–15117,

1802 <https://doi.org/10.5194/acp-16-15097-2016>, 2016.

1803 Ryder, C. L., Highwood, E. J., Rosenberg, P. D., Trembath, J., Brooke, J. K., Bart, M., Dean, A.,

1804 Crosier, J., Dorsey, J., Brindley, H., Banks, J., Marsham, J. H., McQuaid, J. B., Sodemann, H., and

1805 Washington, R.: Optical properties of Saharan dust aerosol and contribution from the coarse mode

1806 as measured during the Fennec 2011 aircraft campaign, *Atmospheric Chemistry and Physics*, 13,

1807 303–325, <https://doi.org/10.5194/acp-13-303-2013>, 2013.

1808 Ryu, Y.-H. and Min, S.-K.: Improving Wet and Dry Deposition of Aerosols in WRF-Chem: Updates to

1809 Below-Cloud Scavenging and Coarse-Particle Dry Deposition, *Journal of Advances in Modeling*

1810 *Earth Systems*, 14, e2021MS002792, <https://doi.org/10.1029/2021MS002792>, 2022.

1811 Shangguan, W., Dai, Y., Duan, Q., Liu, B., and Yuan, H.: A global soil data set for earth system

1812 modeling, *Journal of Advances in Modeling Earth Systems*, 6, 249–263,

1813 <https://doi.org/10.1002/2013MS000293>, 2014.

1814 Shao, Y. and Lu, H.: A simple expression for wind erosion threshold friction velocity, *Journal of*

1815 *Geophysical Research: Atmospheres*, 105, 22437–22443, <https://doi.org/10.1029/2000JD900304>,

1816 2000.

1817 Singh, I., Martin, R. V., Bindle, L., Chatterjee, D., Li, C., Oxford, C., Xu, X., and Wang, J.: Effect of

1818 Dust Morphology on Aerosol Optics in the GEOS-Chem Chemical Transport Model, on UV-Vis Trace

1819 Gas Retrievals, and on Surface Area Available for Reactive Uptake, *Journal of Advances in Modeling*

1820 *Earth Systems*, 16, e2023MS003746, <https://doi.org/10.1029/2023MS003746>, 2024.

1821 [Sinyuk, A., Torres, O., and Dubovik, O.: Combined use of satellite and surface observations to infer](https://doi.org/10.1029/2002GL016189)

1822 [the imaginary part of refractive index of Saharan dust, *Geophysical Research Letters*, 30,](https://doi.org/10.1029/2002GL016189)

1823 [https://doi.org/10.1029/2002GL016189, 2003.](https://doi.org/10.1029/2002GL016189)

Formatted: Normal

Deleted: <https://doi.org/10.1029/2023MS003746>,

1825 [Smith, R. J.: Use and misuse of the reduced major axis for line-fitting, *American Journal of Physical*](#)
1826 [Anthropology, 140, 476–486, <https://doi.org/10.1002/ajpa.21090>, 2009.](#)

1827 Snider, G., Weagle, C. L., Martin, R. V., van Donkelaar, A., Conrad, K., Cunningham, D., Gordon, C.,
1828 Zwicker, M., Akoshile, C., Artaxo, P., Anh, N. X., Brook, J., Dong, J., Garland, R. M., Greenwald, R.,
1829 Griffith, D., He, K., Holben, B. N., Kahn, R., Koren, I., Lagrosas, N., Lestari, P., Ma, Z., Vanderlei
1830 Martins, J., Quel, E. J., Rudich, Y., Salam, A., Tripathi, S. N., Yu, C., Zhang, Q., Zhang, Y., Brauer, M.,
1831 Cohen, A., Gibson, M. D., and Liu, Y.: SPARTAN: a global network to evaluate and enhance satellite-
1832 based estimates of ground-level particulate matter for global health applications, *Atmospheric*
1833 *Measurement Techniques*, 8, 505–521, <https://doi.org/10.5194/amt-8-505-2015>, 2015.

1834 [Song, Q., Zhang, Z., Yu, H., Ginoux, P., and Shen, J.: Global dust optical depth climatology derived](#)
1835 [from CALIOP and MODIS aerosol retrievals on decadal timescales: regional and interannual](#)
1836 [variability, *Atmospheric Chemistry and Physics*, 21, 13369–13395, \[https://doi.org/10.5194/acp-21-\]\(https://doi.org/10.5194/acp-21-13369-2021\)](#)
1837 [13369-2021](#), 2021.

1838 Swap, R., Garstang, M., Greco, S., Talbot, R., and Kallberg, P.: Saharan dust in the Amazon Basin,
1839 *Tellus B*, 44, 133–149, <https://doi.org/10.1034/j.1600-0889.1992.t01-1-00005.x>, 1992.

1840 [Swenson, S. C. and Lawrence, D. M.: Assessing a dry surface layer-based soil resistance](#)
1841 [parameterization for the Community Land Model using GRACE and FLUXNET-MTE data, *Journal of*](#)
1842 [Geophysical Research: Atmospheres](#), 119, 10,299–10,312, <https://doi.org/10.1002/2014JD022314>,
1843 [2014.](#)

1844 The International GEOS-Chem User Community: geoschem/GCHP: GCHP 14.4.1.,
1845 <https://doi.org/10.5281/zenodo.12584305>, 2024.

1846 Tian, R., Ma, X., and Zhao, J.: A revised mineral dust emission scheme in GEOS-Chem:
1847 improvements in dust simulations over China, *Atmospheric Chemistry and Physics*, 21, 4319–
1848 4337, <https://doi.org/10.5194/acp-21-4319-2021>, 2021.

1849 [Tindan, J. Z., Jin, Q., and Pu, B.: Understanding day–night differences in dust aerosols over the dust](#)
1850 [belt of North Africa, the Middle East, and Asia, *Atmos. Chem. Phys.*, 23, 5435–5466,](#)
1851 <https://doi.org/10.5194/acp-23-5435-2023>, 2023.

1852 Uno, I., Wang, Z., Chiba, M., Chun, Y. S., Gong, S. L., Hara, Y., Jung, E., Lee, S.-S., Liu, M., Mikami,
1853 M., Music, S., Nickovic, S., Satake, S., Shao, Y., Song, Z., Sugimoto, N., Tanaka, T., and Westphal,

1854 D. L.: Dust model intercomparison (DMIP) study over Asia: Overview, *Journal of Geophysical*
1855 *Research: Atmospheres*, 111, <https://doi.org/10.1029/2005JD006575>, 2006.

1856 Wang, Q., Jacob, D. J., Fisher, J. A., Mao, J., Leibensperger, E. M., Carouge, C. C., Le Sager, P.,
1857 Kondo, Y., Jimenez, J. L., Cubison, M. J., and Doherty, S. J.: Sources of carbonaceous aerosols and
1858 deposited black carbon in the Arctic in winter-spring: implications for radiative forcing,
1859 *Atmospheric Chemistry and Physics*, 11, 12453–12473, [https://doi.org/10.5194/acp-11-12453-](https://doi.org/10.5194/acp-11-12453-2011)
1860 2011, 2011.

1861 Wang, Q., Jacob, D. J., Spackman, J. R., Perring, A. E., Schwarz, J. P., Moteki, N., Marais, E. A., Ge,
1862 C., Wang, J., and Barrett, S. R. H.: Global budget and radiative forcing of black carbon aerosol:
1863 Constraints from pole-to-pole (HIPPO) observations across the Pacific, *Journal of Geophysical*
1864 *Research: Atmospheres*, 119, 195–206, <https://doi.org/10.1002/2013jd020824>, 2014a.

1865 Wang, X., Zhang, L., and Moran, M. D.: Development of a new semi-empirical parameterization for
1866 below-cloud scavenging of size-resolved aerosol particles by both rain and snow, *Geoscientific*
1867 *Model Development*, 7, 799–819, <https://doi.org/10.5194/gmd-7-799-2014>, 2014b.

1868 Wang, X., Jacob, D. J., Downs, W., Zhai, S., Zhu, L., Shah, V., Holmes, C. D., Sherwen, T., Alexander,
1869 B., Evans, M. J., Eastham, S. D., Neuman, J. A., Veres, P. R., Koenig, T. K., Volkamer, R., Huey, L. G.,
1870 Bannan, T. J., Percival, C. J., Lee, B. H., and Thornton, J. A.: Global tropospheric halogen (Cl, Br, I)
1871 chemistry and its impact on oxidants, *Atmospheric Chemistry and Physics*, 21, 13973–13996,
1872 <https://doi.org/10.5194/acp-21-13973-2021>, 2021.

1873 Webb, N. P., Chappell, A., LeGrand, S. L., Ziegler, N. P., and Edwards, B. L.: A note on the use of
1874 drag partition in aeolian transport models, *Aeolian Research*, 42, 100560,
1875 <https://doi.org/10.1016/j.aeolia.2019.100560>, 2020.

1876 Weng, H., Lin, J., Martin, R. V., Millet, D. B., Jaeglé, L., Ridley, D., Keller, C., Li, C., Du, M., and Meng,
1877 J.: Global high-resolution emissions of soil NO_x, sea salt aerosols, and biogenic volatile organic
1878 compounds, *Scientific Data*, 7, 148, <https://doi.org/10.1038/s41597-020-0488-5>, 2020.

1879 Wu, C., Lin, Z., and Liu, X.: The global dust cycle and uncertainty in CMIP5 (Coupled Model
1880 Intercomparison Project phase 5) models, *Atmospheric Chemistry and Physics*, 20, 10401–10425,
1881 <https://doi.org/10.5194/acp-20-10401-2020>, 2020.

1882 Wu, C., Lin, Z., Shao, Y., Liu, X., and Li, Y.: Drivers of recent decline in dust activity over East Asia,

1883 Nature Communications, 13, 7105, <https://doi.org/10.1038/s41467-022-34823-3>, 2022.

1884 Young, S. A., Vaughan, M. A., Garnier, A., Tackett, J. L., Lambeth, J. D., and Powell, K. A.: Extinction
 1885 and optical depth retrievals for CALIPSO's Version 4 data release, Atmospheric Measurement
 1886 Techniques, 11, 5701–5727, <https://doi.org/10.5194/amt-11-5701-2018>, 2018.

1887 [Yu, Y., Kalashnikova, O. V., Garay, M. J., Lee, H., Choi, M., Okin, G. S., Yorks, J. E., Campbell, J. R.,
 1888 and Marquis, J.: A global analysis of diurnal variability in dust and dust mixture using CATS
 1889 observations, Atmos. Chem. Phys., 21, 1427–1447, <https://doi.org/10.5194/acp-21-1427-2021>,
 1890 2021.](#)

1891 Yuan, H., Dai, Y., Xiao, Z., Ji, D., and Shangguan, W.: Reprocessing the MODIS Leaf Area Index
 1892 products for land surface and climate modelling, Remote Sensing of Environment, 115, 1171–1187,
 1893 <https://doi.org/10.1016/j.rse.2011.01.001>, 2011.

1894 Zender, C. S., Bian, H., and Newman, D.: Mineral Dust Entrainment and Deposition (DEAD) model:
 1895 Description and 1990s dust climatology, Journal of Geophysical Research: Atmospheres, 108,
 1896 <https://doi.org/10.1029/2002JD002775>, 2003.

1897 Zhang, D.: Improving Fine Mineral Dust Representation from the Surface to the Column in GEOS-
 1898 Chem version 14.4.1, <https://doi.org/10.5281/zenodo.14510793>, 2024.

1899 Zhang, J. and Shao, Y.: A new parameterization of particle dry deposition over rough surfaces,
 1900 Atmospheric Chemistry and Physics, 14, 12429–12440, [https://doi.org/10.5194/acp-14-12429-](https://doi.org/10.5194/acp-14-12429-2014)
 1901 2014, 2014.

1902 Zhang, L., Gong, S., Padro, J., and Barrie, L.: A size-segregated particle dry deposition scheme for
 1903 an atmospheric aerosol module, Atmospheric Environment, 35, 549–560,
 1904 [https://doi.org/10.1016/S1352-2310\(00\)00326-5](https://doi.org/10.1016/S1352-2310(00)00326-5), 2001.

1905 Zhang, L., Kok, J. F., Henze, D. K., Li, Q., and Zhao, C.: Improving simulations of fine dust surface
 1906 concentrations over the western United States by optimizing the particle size distribution,
 1907 Geophysical Research Letters, 40, 3270–3275, <https://doi.org/10.1002/grl.50591>, 2013.

1908 [Zhao, A., Ryder, C. L., and Wilcox, L. J.: How well do the CMIP6 models simulate dust aerosols?,
 1909 Atmos. Chem. Phys., 22, 2095–2119, <https://doi.org/10.5194/acp-22-2095-2022>, 2022.](#)

1910 Zhu, H., Martin, R. V., Croft, B., Zhai, S., Li, C., Bindle, L., Pierce, J. R., Chang, R. Y.-W., Anderson, B.

1911 E., Ziemba, L. D., Hair, J. W., Ferrare, R. A., Hostetler, C. A., Singh, I., Chatterjee, D., Jimenez, J. L.,
1912 Campuzano-Jost, P., Nault, B. A., Dibb, J. E., Schwarz, J. S., and Weinheimer, A.: Parameterization
1913 of size of organic and secondary inorganic aerosol for efficient representation of global aerosol
1914 optical properties, *Atmospheric Chemistry and Physics*, 23, 5023–5042,
1915 <https://doi.org/10.5194/acp-23-5023-2023>, 2023.

1916

Font: +Body (Aptos)